



## Research papers

## Fe–Si-oxyhydroxide deposits at a slow-spreading centre with thickened oceanic crust: The Lilliput hydrothermal field (9°33'S, Mid-Atlantic Ridge)

Vesselin M. Dekov<sup>a,\*</sup>, Sven Petersen<sup>b</sup>, C.-Dieter Garbe-Schönberg<sup>c</sup>, George D. Kamenov<sup>d</sup>, Mirjam Perner<sup>e</sup>, Ernő Kuzmann<sup>f</sup>, Mark Schmidt<sup>b</sup>

<sup>a</sup> Department of Geology and Paleontology, University of Sofia, 15 Tsar Osvoboditel Blvd., 1000 Sofia, Bulgaria

<sup>b</sup> Leibniz-Institut fuer Meereswissenschaften, IFM-GEOMAR, Wischhofstr. 1-3, D-24148 Kiel, Germany

<sup>c</sup> Institut fuer Geowissenschaften, Abt. Geologie, Universitaet Kiel, Olshausenstr. 40, D-24118 Kiel, Germany

<sup>d</sup> Department of Geological Sciences, University of Florida, 241 Williamson Hall, Gainesville, FL 32611, USA

<sup>e</sup> Microbiology and Biotechnology Unit, University of Hamburg, Ohnhorststr. 18, D-22609 Hamburg, Germany

<sup>f</sup> Laboratory of Nuclear Chemistry, Hungarian Academy of Sciences Chemical Research Center, Eötvös University, 1/A Pázmány P., Budapest H-1117, Hungary

## ARTICLE INFO

## Article history:

Received 15 May 2010

Received in revised form 17 September 2010

Accepted 20 September 2010

Editor: J. Fein

## Keywords:

Fe–Si-oxyhydroxides

Geochemistry

Hydrothermal

Lilliput vent field

Mid-Atlantic Ridge

## ABSTRACT

Diffuse and focused low-temperature fluids emanate at 9°33'S (Mid-Atlantic Ridge) and precipitate Fe–Si-oxyhydroxides that form chimneys, mounds and flat-lying deposits. This extensive vent field, named Lilliput, lies at the axial zone of a spreading segment with a significantly thickened crust (~11 km). Theoretically much more heat needs to be removed from a thick-crust spreading center compared to a spreading center with typical thickness of ~6 km. Therefore, settings with thickened crust should be favourable for supporting very powerful hydrothermal systems capable of producing large mineral deposits. This is the first report on the composition of seafloor hydrothermal deposits at abnormally thickened oceanic crust due to hotspot–ridge interaction. Our studies revealed that generally the Lilliput hydrothermal deposits are very similar in morphology, structure, composition and lateral extent to other low-temperature hydrothermal deposits of mid-ocean ridges and intraplate volcanoes. Deposits at the Lilliput vent field are composed of Si-containing goethite and ferrihydrite, have very low contents of a number of transition and rare earth elements and show REE distribution patterns with negative Ce and Eu anomalies. The speciation and precipitation of the main deposit-forming elements, Fe and Si, at the hydrothermal field appear to be partially controlled by live microbes and exuded organic compounds. The  $\delta^{18}\text{O}$  values of the precipitated silica-containing Fe-oxyhydroxides point to low-temperature formation and Sr–Nd–Pb-isotope variations suggest that the hydrothermal precipitates scavenged metals predominantly from the ambient seawater. These findings are in agreement with the biogeochemical scenario for their precipitation.

© 2010 Elsevier B.V. All rights reserved.

### 1. Introduction

Seafloor hydrothermal activity at mid-ocean ridges (MOR), intra-oceanic arcs and hotspots is one of the fundamental processes controlling the transfer of heat and chemical species between the lithosphere and the ocean (Elderfield and Schultz, 1996; German and Von Damm, 2004). Seafloor hydrothermal systems are also of biological importance because they support unique and rich ecosystems. The biology in turn can affect precipitation of minerals. The MOR chain transects all ocean basins on Earth, and the diverse geological conditions of submarine tectonic extension generate a great variety of hydrothermal vents and deposits. Since their discovery in 1977 (Corliss et al., 1979; Spiess et al., 1980), scientists have investigated more than 200 seafloor vent fields (Hannington et al., 2005). However, the search for

hydrothermal sites has largely been constrained to the northern Atlantic and Pacific Oceans. Vast segments of the MOR in the South Atlantic, Indian, and Arctic Oceans remain virtually unexplored for hydrothermal activity. These underexplored segments of the global MOR system largely correspond to spreading centers where the tectonic extension rates are very slow, and where lithospheric extension may be accommodated by stable fault slip as opposed to volcanic accretion (e.g., Dick et al., 2003). Based on seismic investigations some of these slow-spreading centers are known to have thickened crust (~10 km), as a result of high magma production due to hotspot–ridge interaction. Therefore, this type of setting may be expected to support very active and high-power hydrothermal systems, which can generate large mineral deposits as theoretically, much more heat has to be transported away from a thick-crust spreading center than from a spreading center with a typical thickness of ~6 km. On the other hand, a crustal thermal model (Chen, 2003) suggests that the thicker, hotter, more ductile crust associated with hotspot-affected spreading centers has a substantially reduced depth of brittle fracturing and consequent depth of seawater

\* Corresponding author. Tel.: +359 2 9308 276; fax: +359 2 9446 487.  
E-mail address: [dekov@gea.uni-sofia.bg](mailto:dekov@gea.uni-sofia.bg) (V.M. Dekov).

penetration. Hence, it might be expected that the hotspot stifles convective hydrothermal cooling.

More than 40 hotspots are known to date (Richards et al., 1988). Some of them lie as close to a MOR axis (<500 km) as to influence its morphology (Ito and Lin, 1995). It appears that those ridge stretches affected by a hotspot represent ~20% of the global MOR chain, but very little is still known about hotspot influence on the distribution and composition of hydrothermal fields along the MOR. Despite intense exploration efforts seafloor hydrothermal activity has been detected (plume and deep-towed camera surveys) only on three of these hotspot–ridge intersections: the Iceland hotspot–Reykjanes Ridge (German et al., 1994), the Amsterdam–St. Paul hotspot–Southeast Indian Ridge (Johnson et al., 2000), and the Galápagos hotspot–Galápagos spreading center (GSC) (Baker et al., 2008). The first two fields appear unusually deficient in hydrothermal activity compared

with that at the GSC with clear evidence for high-temperature hydrothermal vents. All they have abnormally thickened oceanic crust: >8 km. However, there are no reports on the composition of hydrothermal deposits of any of them to date. The surprising rarity of hydrothermal activity at such spreading centers motivated our efforts to seek hydrothermal sites hosted by thickened crust in other areas along the mid-ocean ridges.

The recent discovery of low-temperature hydrothermal venting at a spreading center near 9°30'S on the slow-spreading Mid-Atlantic Ridge (MAR) has shown that such thickened (~11 km) oceanic crust can host hydrothermal systems (Haase et al., 2009; Fig. 1) that might be different from their thin-crust counterparts.

Here we report on the mineralogy and geochemistry of the low-temperature deposits from this new hydrothermal system (Lilliput field, 9°33'S MAR), and propose possible scenarios for their formation.

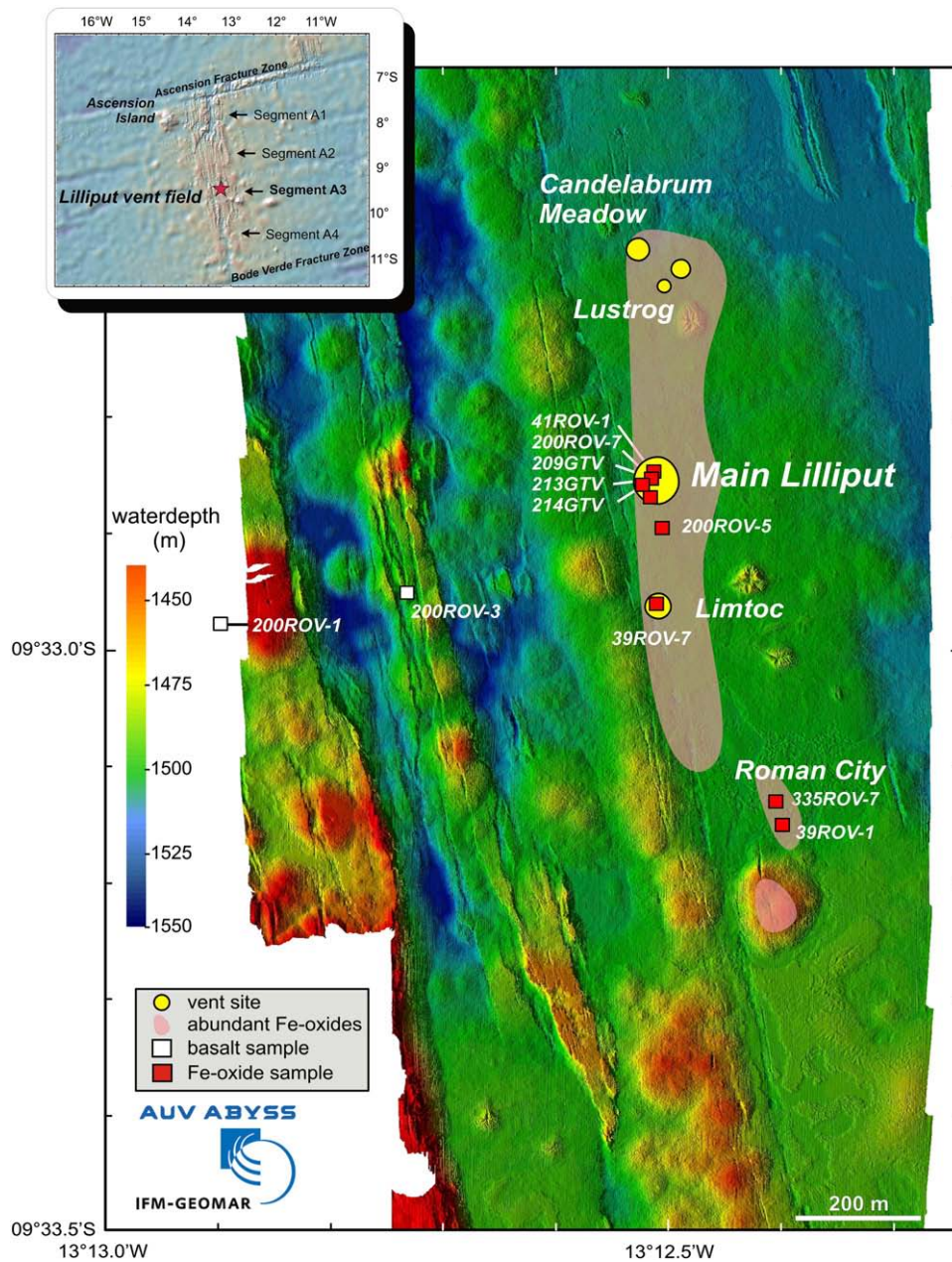


**Fig. 1.** Bathymetric map (AUV high-resolution multi-beam mapping; RESON SEABAT 7125) of the volcanically active part of segment A3 of the MAR between the Ascension and Bode Verde Fracture Zones (inset map) showing the hydrothermal vent sites and sampling sites at the Lilliput vent field. Note the row of pillow mounds forming an axial volcanic ridge, the parallel fissures east of the ridge and the faulted western rift flank. The five currently known diffuse hydrothermal vent sites occur east of the volcanic ridge within a flat area interpreted as a young lava flow (Haase et al., 2009).

## 2. Geological setting

The MAR between the Ascension and the Bode Verde fracture zones has been explored for recent volcanic events and related hydrothermal activity during three cruises of the R/V *Meteor* (M64/1 in 2005, M68/1 in 2006 and M78/2 in 2009) (Haase et al., 2009). Previous geophysical studies of the MAR between these major fracture zones estimated that the full spreading rate is 32–33 mm/yr (DeMets et al., 1994) and established that the ridge consists of 4 segments termed A1 to A4 (Minshull et al., 1998; Bruguier et al., 2003) (Fig. 1). The considerable gravity anomalies along these ridge segments have been attributed (Bruguier et al., 2003) to variations in crustal thickness. The Lilliput hydrothermal field, which was discovered during hydrothermal plume exploration, ROV dives and AUV mapping at 9°33'S MAR (Fig. 1), lies at segment A3. This segment has experienced ridge jumps since ~1 Ma, it is the shallowest of the 4 segments and is characterized by a 70 km long axial high with 2 large off-axis seamounts located east of the ridge axis (Brozena, 1986). It has a significantly thickened crust

of ~11 km (gravimetric modelling; Bruguier et al., 2003). The size and shape of segment A3 are similar to the volcanically and hydrothermally active CoAxial Segment on the Juan de Fuca Ridge, which lies at the intersection of the ridge with the Cobb–Eickelberg Seamount Chain (Canadian-American Seamount Expedition, 1985). The ridge segment A3 therefore resembles rather a fast spreading centre with a neovolcanic zone occurring on a shallow ridge with a narrow cleft than a deep rift typical for the slow-spreading MAR.

The Lilliput hydrothermal field is located on the northern flank of the segment A3 axial high (water depth ~1500 m). The plate boundary at this hydrothermal field is characterized by an ~800 m wide axial trough bounded by faults with scarps of 10 to 20 m in height. A 100–200 m wide ridge consisting of numerous small pillow mounds up to about 30 m high lies in the centre of this trough. The volcanic ridge is supposed to represent the surface expression of an underlying dike, which fed the flow (Haase et al., 2009). A depression about 20 m wide and at least 2 km long occurs at the eastern base of this volcanic ridge and is often partially buried by the volcanic mounds. The background

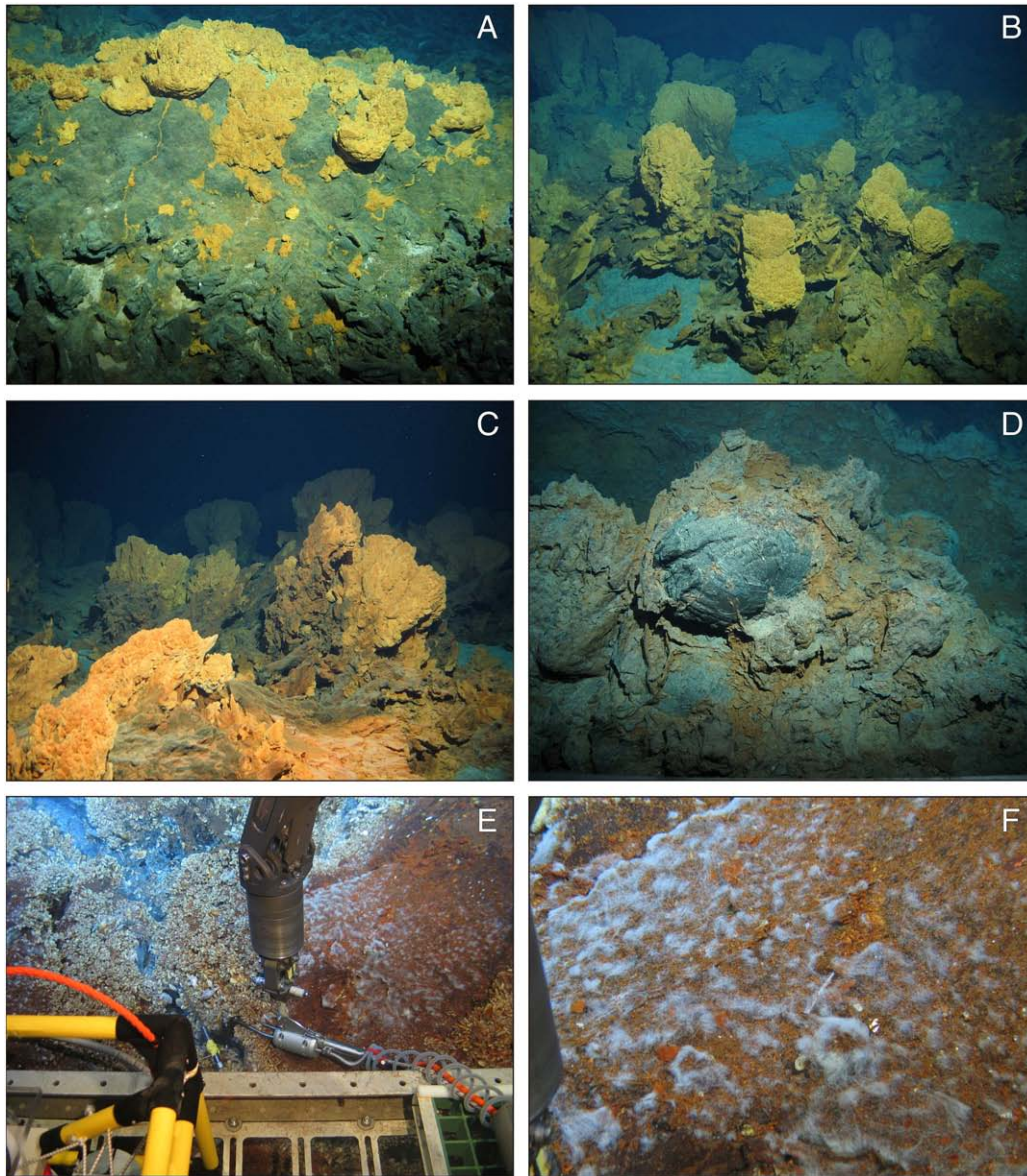


**Fig. 2.** Lilliput hydrothermal deposits: (A), (B) yellow, clump-like structures on basalt flows; (C) red to reddish-brown, bush-like, feathery structures; (D) red-brown deposits among basalt pillows; (E) area of low-temperature diffuse venting (T-10 °C) in the Main Lilliput field: note the abundant small mussels and the white bacterial mats associated with the Fe-Si-oxyhydroxides to the right; (F) close-up of panel E showing white bacterial mats on orange-red deposit.

sedimentation rate at this area is ~32 mm/kyr (Ruddiman and Janecek, 1989). Five low-temperature hydrothermal sites (Candelabrum Meadow, Lustrog, Main Lilliput, Limtoc and Roman City) are currently known along the eastern flank of this depression (water depths 1494–1505 m) on a large, young (<100 years old; Haase et al., 2009) lava flow (Fig. 1). They comprise abundant yellow, clump-like (Fig. 2A, B) to red-brown, bush-like, feathery structures (Fig. 2C) clustering along fissures on the basalt flows. Red to red-brown deposits fill the space among basalt pillows (Fig. 2D) or form small knolls. These deposits are soft and fragile. White bacterial mats often develop on their surface (Fig. 2E, F). Venting is low-temperature (4.8°–17.6 °C, measured with a probe inserted by the ROV's manipulator into fissures and small orifices; Fig. 2E) and diffuse: from both cracks within basalt flows and vent structures. It is considered to be related to the young diking and eruption event (Haase et al., 2009). The vent fluids are reducing and slightly acidic (pH = 5.9–7.2). The Mg concentrations in vent fluids are slightly lower than those in seawater indicating that the diffuse fluids consist of a few percent of hydrothermal end-member fluid mixed with ambient seawater. The Si concentrations in them (0.06–0.54 mmol/l; Haase et al., 2009) are significantly increased relative to the Si content of the ambient seawater (<0.01 mmol/l). Dissolved Fe concentrations (0.1–43 μmol/l) correlate with fluid temperatures. While in most samples total H<sub>2</sub>S was <50 μmol/l, the sample with the highest temperature had 341 μmol/l H<sub>2</sub>S (the maximum H<sub>2</sub>S concentrations measured were 500 μmol/l; Perner et al., 2007). The vent fluids have CH<sub>4</sub> concentrations elevated over the background values and very low H<sub>2</sub>/CH<sub>4</sub> ratios.

Analyses of the bacterial community from the hydrothermal fluids emanating through mussel patches, which cover the red deposits, have demonstrated a very high phylogenetic diversity (Perner et al., 2007). Detected bacteria included *Thiomicrospira* spp. and *Epsilonproteobacteria* (Perner et al., 2007), where the closest cultured representatives are known to oxidize reduced sulfur compounds (cf. Campbell et al., 2006; Nakagawa and Takai, 2008). No bacteria were

detected, which could be related to species typically known to oxidize H<sub>2</sub>, CH<sub>4</sub> or Fe<sup>2+</sup> (Perner et al., 2007). However, a considerable fraction of the detected bacteria were only distantly related to cultured species, with known physiological properties. The macrofauna at the Lilliput hydrothermal field largely consists of small and apparently juvenile bivalves and gastropods which did not show any visible growth during the 4 years of continuing observations (Haase et al., 2009). This possibly reflects the low and intermittent hydrothermal activity and was the reason for the name of the field.

### 3. Materials and methods

We investigated samples from 9 sites of hydrothermal deposition (vents, mounds and sediment) within 3 hydrothermal areas (Main Lilliput, Limtoc and Roman City) of the Lilliput field (Table 1; Fig. 1). One sample (M64/1 209GTV) was split into 2 subsamples (-a and -b) based on macroscopic differences. The main part of the samples obtained (Table 1) were fragments of hydrothermal structures (Fig. 3A). These fragments exhibit complex textures of thin (several millimeters), fragile, folded crust-like layers forming channel-like and chamber-like structures (Fig. 3A). Upon drying at room temperature (~20 °C) for several days they start wasting. Rarely, thin black films were observed on the surface of these yellow to red fragments. In an attempt to select and further study these black films we gently washed the yellow to red material that composes the bulk of the samples (M64/1 213GTV and M64/1 214GTV) away with distilled water and got black residues composed of thin, black flakes (M64/1 213GTV-3 and M64/1 214GTV-3; Fig. 3B). Four basalt samples (2 from young flows close to the axial extrusive zone and 2 from old flows at some distance from it) (Table 1; Fig. 1) were studied along with the other samples for Sr–Nd–Pb isotopes only.

Small (~1 × 1 cm) pieces of wet samples were dried at lab temperature (~20 °C) for a week, mounted on aluminum stubs using carbon tapes, coated with Au–Pd and investigated with a Scanning

**Table 1**  
Investigated samples from the Lilliput hydrothermal field (Mid-Atlantic Ridge).

Sample #	Locality	Latitude (S)	Longitude (W)	Depth (m)	Sampling device	Hand sample description	Mineralogy (XRD data)
<i>Fe–Si–oxyhydroxides</i>							
M64/1 200ROV-5	Main Lilliput	09°32.90'	13°12.50'	1494	ROV, net	Red deposits (containing small basalt shards and micromorphic bivalves) in between pillow lava.	X-ray amorphous Fe–Si–oxyhydroxides
M64/1 200ROV-7	Main Lilliput	09°32.86'	13°12.53'	1495	ROV, shovel	Thick, red cover on top of pillow lava.	X-ray amorphous Fe–Si–oxyhydroxides, goethite
M64/1 209GTV-a	Main Lilliput	09°32.86'	13°12.52'	1511	TV-grab	Red to red-orange, fragile crust-like fragments of chimney.	X-ray amorphous Fe–Si–oxyhydroxides, goethite
M64/1 209GTV-b	Main Lilliput	09°32.86'	13°12.52'	1511	TV-grab	Yellow-orange, soft, fragile crust-like fragments of chimney.	goethite, X-ray amorphous Fe–Si–oxyhydroxides
M64/1 213GTV	Main Lilliput	09°32.83'	13°12.54'	1513	TV-grab	Red to orange crust-like fragments of chimney.	goethite, X-ray amorphous Fe–Si–oxyhydroxides
M64/1 213GTV-3	Main Lilliput	09°32.83'	13°12.54'	1513	TV-grab	Thin, black flakes selected from bulk sample M64/1 213GTV.	marcasite, pyrite
M64/1 214GTV	Main Lilliput	09°32.84'	13°12.53'	1511	TV-grab	Red to orange crust-like fragments of chimney.	goethite, X-ray amorphous Fe–Si–oxyhydroxides
M64/1 214GTV-3	Main Lilliput	09°32.84'	13°12.53'	1511	TV-grab	Thin, black flakes selected from bulk sample M64/1 214GTV.	marcasite, pyrite
M68/1 39ROV-1	Roman City	09°33.15'	13°12.42'	1486	ROV, shovel	Red sediment.	X-ray amorphous Fe–Si–oxyhydroxides
M68/1 39ROV-7A	Limtoc	09°32.96'	13°12.51'	1494	ROV, bionet	Dark-red crusts (chimney fragments?) containing rare micromorphic bivalves and gastropods.	X-ray amorphous Fe–Si–oxyhydroxides, goethite
M68/1 41ROV-1	Main Lilliput	09°32.85'	13°12.54'	1495	ROV, net	Red sediment with small, white particles: micromorphic bivalves (?), forams (?).	goethite, X-ray amorphous Fe–Si–oxyhydroxides
M78/2 335ROV-7	Roman City	09°33.13'	13°12.43'	1493	ROV, claw	Red, fragile crust-like fragments of chimney.	X-ray amorphous Fe–Si–oxyhydroxides
<i>Basalts</i>							
M64/1 194ROV-13	–	09°34.38'	13°12.36'	1468	ROV, claw	Young, aphyric basalt sheet flow.	–
M64/1 194ROV-4	–	09°34.38'	13°12.84'	1429	ROV, claw	Old, aphyric pillow basalt.	–
M64/1 200ROV-3	–	09°32.88'	13°12.72'	1505	ROV, claw	Young, aphyric basalt lobate flow.	–
M64/1 200ROV-1	–	09°33.00'	13°12.90'	1469	ROV, claw	Old, aphyric pillow basalt.	–

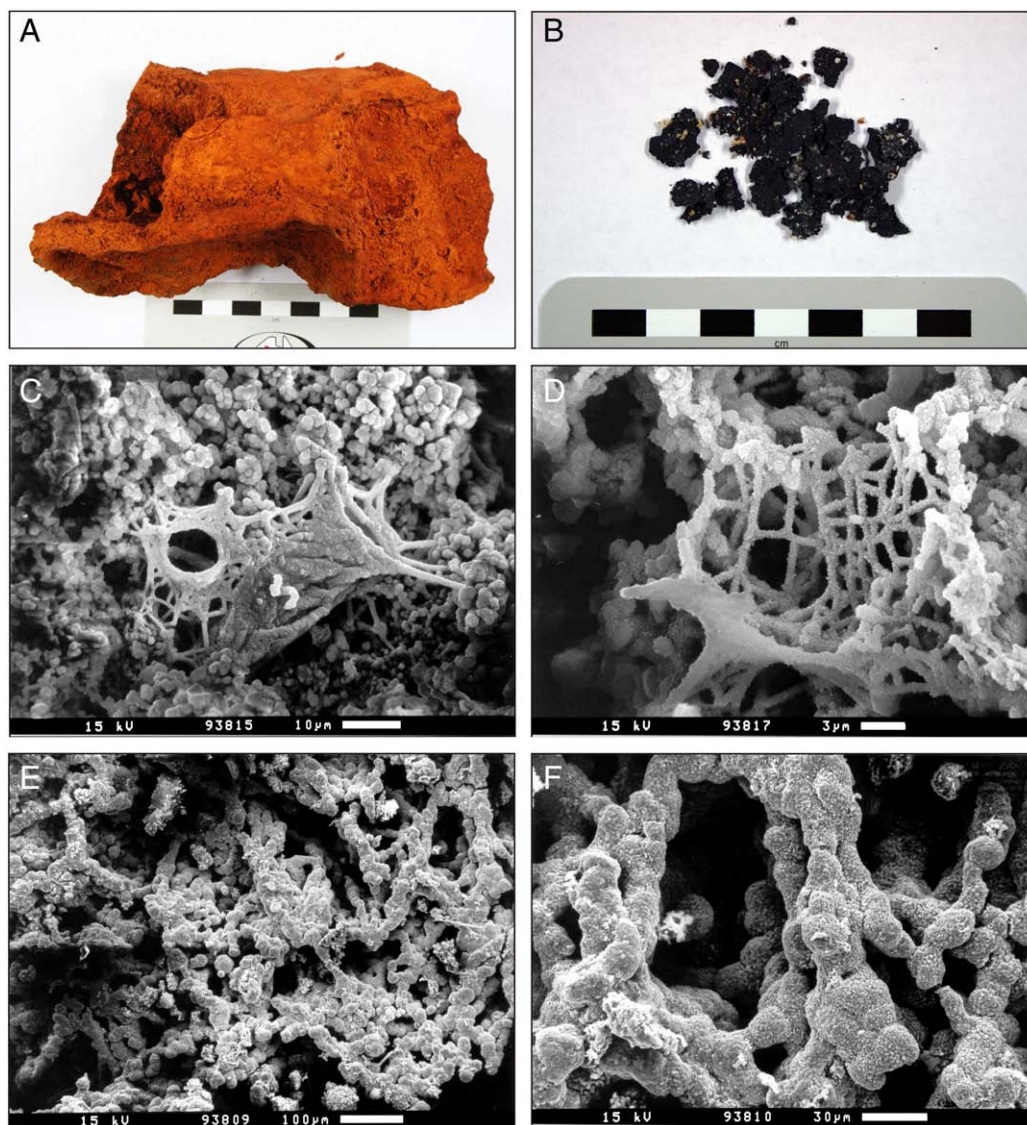


**Fig. 3.** Macro- (A, B) and micro-photographs (SEM secondary-electron images; C, D, E, F) of: (A) fragment of typical hydrothermal structure from the Lilliput vent field (M64/1 209GTV); (B) thin, black flakes composing the residue (M64/1 214GTV-3) after washing out the yellow to red material of bulk sample (M64/1 214GTV); (C) spider net-like and spherical bacterial structures encrusted with FeOOH (EDS data) (M64/1 209GTV); (D) thread-like bacterial structures encrusted with FeOOH (M64/1 209GTV); (E) thread-like bacterial structures encrusted with Fe-sulfide (M64/1 213GTV-3); (F) close-up of the Fe-sulfide-encrusted bacterial structures shown at panel E. Scale bars at A and B in cm.

Electron Microscope (SEM) (CamScan CS44,  $V = 15 \text{ kV}$ ,  $I = 12 \text{ nA}$ , electron beam diameter of  $2 \mu\text{m}$ ).

Subsamples ( $\sim 20 \text{ g}$ ) from all the samples were dried in an oven with laminar air flow at  $30 \text{ }^\circ\text{C}$  for 48 h, ground manually in an agate mortar up to fine powder and used in all the other analyses.

The mineralogy of the samples was studied by: (1) X-ray diffractometry (XRD) (Philips X-ray diffractometer PW 1710 with automatic divergence slit and monochromatic  $\text{Co K}\alpha$  radiation,  $40 \text{ kV}$ ,  $35 \text{ mA}$ ) of random powder mounts: scans from  $5$  to  $80$   $^\circ 2\theta$ , with  $0.01$   $^\circ 2\theta$  step, at  $2 \text{ s/step}$ ; (2) Mössbauer spectroscopy.  $^{57}\text{Fe}$  Mössbauer spectra of powdered samples were recorded by conventional Mössbauer spectrometers (WISSEL) working in constant acceleration mode in transmission geometry at  $293 \text{ K}$  and  $85 \text{ K}$  in a temperature-controlled cryostat (Leybold). A closed circuit refrigerator based cryostat (APD) was used for the measurements between  $25 \text{ K}$  and  $80 \text{ K}$ . A  $50 \text{ mCi}$  activity  $^{57}\text{Co}(\text{Rh})$  source supplied the  $\gamma$  rays for the measurements. The isomer shifts were given relatively to  $\alpha\text{-Fe}$ . The evaluation of the Mössbauer spectra was carried out via the least squares fitting of Lorentzians by the help of the MOSSWINN program (Klencsár et al., 1996).

The chemical composition of the samples was determined by X-ray fluorescence (XRF) spectrometry and Inductively Coupled Plasma Mass Spectrometry (ICP-MS). XRF analyses were performed using Axios XRF spectrometer ( $3 \text{ kW}$ , wavelength dispersive, by PANanalytical). Twelve major elements were analyzed quantitatively after fusion of  $0.1 \text{ g}$  of sample material with  $3.6 \text{ g}$  of dilithium tetraborate at  $1050 \text{ }^\circ\text{C}$  for ca.  $16 \text{ min}$ . The quality of the results was controlled using natural and synthetic certified reference materials (CRM) (i.e., BCR, Community Bureau of Reference, Brussels). This procedure ensured an analytical precision better than  $\pm 0.5\%$  relative for major elements (analytical precision for XRF analyses of certified reference materials). The trace element and rare earth element (REE) composition of the samples was determined by ICP-MS using an AGILENT 7500cs instrument. The samples were dissolved by performing a pressurized HF-HCl-HNO<sub>3</sub>-aqua regia attack (Garbe-Schönberg, 1993). The accuracy of the analyses was monitored using international rock standards BHVO-2, AGV-2, GSPN-2 and Nod A-1. Our values are generally within  $<5\%$  of the recommended values for most elements. The precision of sample duplicates as well as repeated analyses is better than  $5\%$  for most elements.

All reagents used for Sr, Nd and Pb isotope sample preparation were Optima-grade and sample preparation was performed in a class 1000 clean lab, equipped with class 10 laminar flow hoods. Sr, Nd and Pb isotopes were determined on a “Nu-Plasma” MC-ICP-MS, following methods described in Kamenov et al. (2008). The reported  $^{87}\text{Sr}/^{86}\text{Sr}$  ratios are relative to NBS 987  $^{87}\text{Sr}/^{86}\text{Sr} = 0.710246$  ( $\pm 0.000030$ ,  $2\sigma$ ). The reported Nd isotopic compositions are relative to JNdi-1  $^{143}\text{Nd}/^{144}\text{Nd} = 0.512103$  ( $\pm 0.000018$ ,  $2\sigma$ ). The Pb isotope data are relative to the following values of NBS 981:  $^{206}\text{Pb}/^{204}\text{Pb} = 16.937$  ( $\pm 0.004$ ,  $2\sigma$ ),  $^{207}\text{Pb}/^{204}\text{Pb} = 15.490$  ( $\pm 0.003$ ,  $2\sigma$ ), and  $^{208}\text{Pb}/^{204}\text{Pb} = 36.695$  ( $\pm 0.009$ ,  $2\sigma$ ).

Stable O isotope analyses were performed on seven selected bulk samples. The salt-free washed and ground samples were pre-treated by vacuum drying as suggested by Bao and Koch (1999), and Yapp

(1987). The dried powder is then reacted in a Ni-alloy vessel with  $\text{ClF}_3$  at  $550^\circ\text{C}$  generally following the method of Clayton and Mayeda (1963). The released oxygen is converted to  $\text{CO}_2$  at a carbon rod and the  $^{18}\text{O}/^{16}\text{O}$ -ratio of  $\text{CO}_2$  is then determined with a Thermo Finnigan MAT 253. The oxygen isotope ratios are given in the  $\delta$ -notation against V-SMOW. Reproducibility of the fluorination process and subsequent mass spectrometric analysis is in the range of  $\pm 0.2\%$  (Schmidt et al., 1997).

Mat material for biological studies was collected by the fluid pumping system KIPS (Garbe-Schönberg et al., 2006) from a site near the mussel field where red deposits were covered by white filaments (Fig. 2E, F). The mat material (M78/2 319ROV-5) was kept in formaldehyde (2% final concentration) at  $4^\circ\text{C}$  and cell shapes were assessed by transmitted light microscopy (Axio Imager M2, Carl Zeiss).

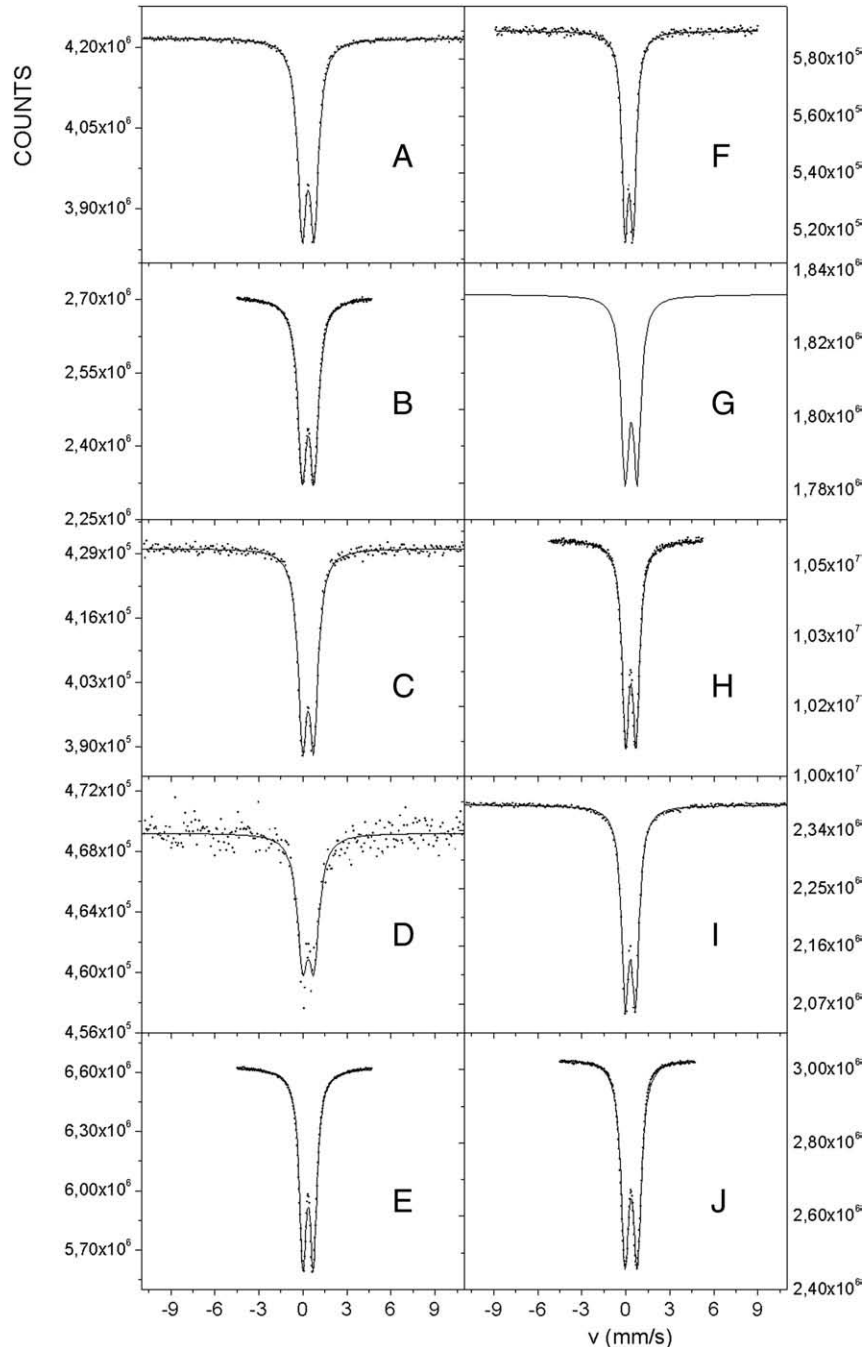


**Fig. 4.** 295 K Mössbauer spectra of samples M64/1 200ROV-5 (A), M64/1 200ROV-7 (B), M64/1 209GTV-a (C), M64/1 209GTV-b (D), M64/1 213GTV (E), M64/1 214GTV (F), M68/1 39ROV-1 (G), M68/1 39ROV-7A (H), M68/1 41ROV-1 (I), and M78/2 335ROV-7 (J).

## 4. Results

### 4.1. Mineralogy of the deposits

The XRD studies coupled with the EDS investigations showed the yellow to red Lilliput deposits were composed of goethite and X-ray amorphous Fe–Si-oxyhydroxides, while the black films on their surfaces are composed of marcasite and pyrite (Table 1). In order to shed more light on the nature of the Fe-oxyhydroxide deposits we performed detailed Mössbauer investigations.

Mössbauer spectra of the Fe-oxyhydroxides recorded at 295 K (room temperature) show no magnetically split subspectra (Fig. 4). The Mössbauer parameters (Table 2) of all the spectra (all with a doublet) are typical for Fe(III) being in paramagnetic state. The isomer shifts of all spectra are identical within the experimental error. They are characteristic for ferrihydrite, but also close to those of well crystalline  $\beta$ -, and  $\gamma$ -Fe(III)-oxyhydroxides (Stevens et al., 1983; Murad and Johnston, 1987; Murad and Cashion, 2004). The quadrupole splitting values have a slight variation within the samples, but their average value is close to that of ferrihydrite (Stevens et al., 1983; Murad and Johnston, 1987; Murad and Cashion, 2004). The relative broad lines indicated with the line-width values are either typical of ferrihydrite (Cornell and Schwertmann, 2006) or can be due to the superposition of subspectra of different species. In order to estimate the possible presence of a superparamagnetic component of any Fe (III)-oxides or -oxyhydroxides the samples were investigated at 85 K (Fig. 5; Table 3). In the Mössbauer spectra recorded at 85 K a magnetically split spectrum component appears besides the doublet subspectrum in the spectra of 5 samples (M64/1 209GTV-b, M64/1 213GTV, M64/1 214GTV, M68/1 39ROV-7A and M68/1 41ROV-1; Fig. 5). These spectra have 42–45 T hyperfine magnetic field,  $-0.21$  to  $-0.24$  mm/s quadrupole splitting, and a line shape typical of goethite (Murad and Cashion, 2004). This magnetic component can be assigned as goethite with small grain size resulting in a superparamagnetic behavior. The 85 K spectra of the other studied samples (M64/1 200ROV-5, M64/1 200ROV-7, M64/1 209GTV-a, M68/1 39ROV-1 and M78/2 335ROV-7) remain doublet, corresponding to the 295 K spectra, that does not indicate goethite presence. The Mössbauer spectrum recorded at 25 K for sample M68/1 41ROV-1 (Fig. 6) confirmed the superparamagnetic goethite: the relative occurrence of the sextet component increases from 60.5% at 85 K to 83.7% at 25 K. The hyperfine field and the quadrupole splitting of the sextet were 50.5 T and  $-0.24$  mm/s, respectively, in good agreement with those characteristic of goethite (Murad and Cashion, 2004). The minor doublet with  $\delta = 0.49$  mm/s,  $\Delta = 0.76$  mm/s,  $W = 0.79$  mm/s can correspond to ferrihydrite (Murad and Cashion, 2004).

XRD (Table 1) and Mössbauer (Table 3) data suggest that goethite (in superparamagnetic state) is the dominant Fe-bearing mineral in

samples M64/1 209GTV-b, M64/1 213GTV and M68/1 41ROV-1. Superparamagnetic goethite with about the same small grain size as in the above mentioned samples could not be found in the samples M64/1 200ROV-5, M64/1 200ROV-7, M64/1 209GTV-a, M68/1 39ROV-1 and M78/2 335ROV-7. However, a small amount of superparamagnetic goethite (i.e., having even smaller grain size) which superparamagnetic transition temperature lower than 85 K cannot be entirely excluded exists in the samples where XRD indicated goethite as minor phase (Table 1). Ferrihydrite is the main Fe-bearing mineral in the samples M64/1 200ROV-5, M64/1 200ROV-7, M64/1 209GTV-a, M68/1 39ROV-1 and M78/2 335ROV-7 and occurs as minor phase in samples M64/1 209GTV-b, M64/1 213GTV, M64/1 214GTV, M68/1 39ROV-7A and M68/1 41ROV-1 (Table 3). The occurrence of another minor superparamagnetic Fe-oxyhydroxide as well as Fe-containing silicate cannot be entirely excluded. No Fe(II)-containing mineral could be detected (Mössbauer data).

### 4.2. Geochemistry of the deposits

Geochemical studies (Table 4) of the Lilliput hydrothermal deposits confirmed that the yellow to red precipitates were composed of Fe- and Si-oxyhydroxides with very low Al, Ti and Mn concentrations. Their Fe/Mn ratios are high and vary over a broad range (Table 4). Al/(Al + Fe + Mn) ratios are extremely low ( $<0.005$ ). The Lilliput hydrothermal deposits are very low in a number of trace elements (Cr, Sc, Co, Ni, Cu, Zn, Rb, Zr, Y, Nb, Sn, Cd, Sb, Cs, Ba, Hf, Ta, W, Tl, Pb, and Th) and REE. Only V, Mo and U concentrations are enriched (Table 4). We have used chondrite-normalized REE distribution patterns for the Lilliput hydrothermal deposits in order to easily compare with the possible associated volcanics, hydrothermal fluids and seafloor massive sulfides (all generally normalized to chondrite values). The REE distribution patterns of Lilliput deposits (Fig. 7) exhibit both negative Ce and negative Eu anomalies, and a slight enrichment in light REE (LREE) relative to heavy REE (HREE) (Table 4). The two macroscopically different subsamples (-a and -b) in which we split a sample (M64/1 209GTV) show different chemical compositions: the sample that is richer in Si and slightly depleted in Fe (M64/1 209GTV-b) has lower concentrations of most of the trace elements, but a bit higher contents of REE relative to the other sample (Table 4). The composition of the black films (M64/1 213GTV-3 and M64/1 214GTV-3) observed on the surface of the yellow to red deposits differs from that of their yellow to red counterparts (M64/1 213GTV and M64/1 214GTV): the black films are enriched in Li, Co, Ni, Rb, Mo, Cd, Cs, Tl and depleted in V, Sr, Y, Sb, Ba, REE, W, U relative to the yellow to red precipitates (Table 4). Their REE distribution patterns (Fig. 7) show weaker both negative Ce and negative Eu anomalies than those of their yellow to red counterparts (Table 4). They are almost flat with very slight enrichment in LREE relative to the HREE (Table 4).

Sr, Nd, and Pb isotopic compositions of local basalt samples and hydrothermal oxyhydroxide deposits are presented in Table 5. Local basalts have Sr–Nd–Pb isotopic systematics typical for Mid-Atlantic Ridge MORB from the region (Figs. 8 and 9). Sr isotopic compositions of the Fe–Si-oxyhydroxide deposits are overall indistinguishable from present-day seawater ( $^{87}\text{Sr}/^{86}\text{Sr} = 0.70917$ ). The only exception is sample M64/1 200ROV-7, which has  $^{87}\text{Sr}/^{86}\text{Sr} = 0.70312$ , and therefore is more similar to the basalts than seawater. Nd isotopic compositions of the Fe–Si-oxyhydroxide deposits vary from  $\epsilon_{\text{Nd}} = +7.1$  to  $-8.4$ , indicating possible mixing between seawater/sediment and basalt-derived Nd (Fig. 8). Pb isotopes of the Fe–Si-oxyhydroxide deposits show lower  $^{206}\text{Pb}/^{204}\text{Pb}$  and higher  $^{207}\text{Pb}/^{204}\text{Pb}$  when compared to the local basalts and plot primarily in the Atlantic sediment field (Fig. 9).

The  $\delta^{18}\text{O}$  values, of all measured samples, range between 12.3 and 19.4‰ (Table 5). The  $\text{SiO}_2$  and  $\text{Fe}_2\text{O}_3$  content of these samples range between 9.5–16.3%, and 53.8–66.6%, respectively (Table 4). A slight

**Table 2**  
295 K Mössbauer parameters<sup>a</sup> of hydrothermal precipitates from the Lilliput hydrothermal field (Mid-Atlantic Ridge).

Sample #	A (%)	$\delta$ (mm/s)	$\Delta$ (mm/s)	W (mm/s)
M64/1 200ROV-5	100	0.36	0.82	0.71
M64/1 200ROV-7	100	0.36	0.82	0.71
M64/1 209GTV-a	100	0.35	0.77	0.71
M64/1 209GTV-b	100	0.36	0.78	0.86
M64/1 213GTV	100	0.36	0.78	0.74
M64/1 214GTV	100	0.36	0.78	0.71
M68/1 39ROV-1	100	0.36	0.81	0.62
M68/1 39ROV-7A	100	0.35	0.71	0.58
M68/1 41ROV-1	100	0.36	0.72	0.67
M78/2 335ROV-7	100	0.36	0.84	0.66

<sup>a</sup> A = line area,  $\delta$  = isomer shift,  $\Delta$  = quadrupole splitting, W = line-width.

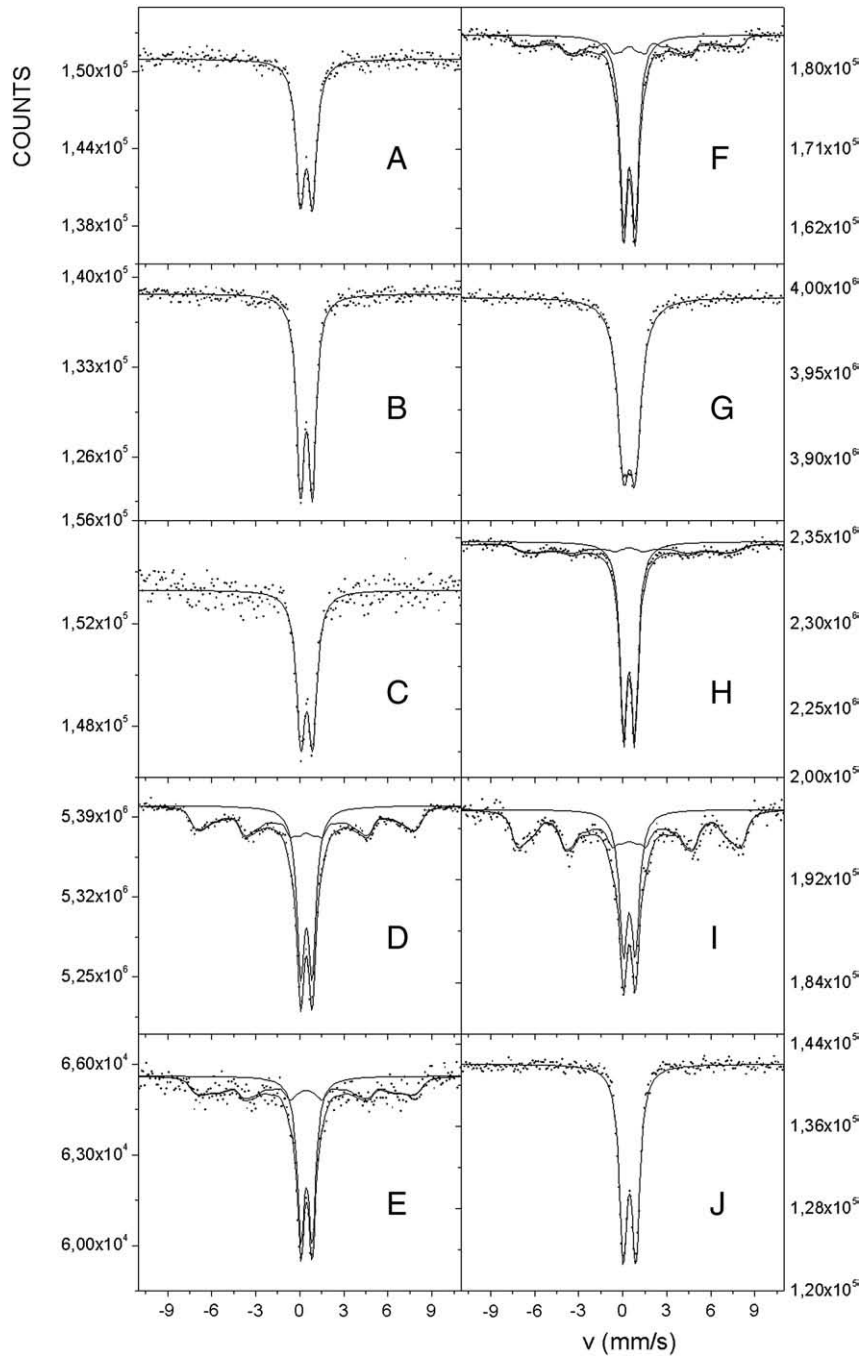


**Fig. 5.** 85 K Mössbauer spectra of samples M64/1 200ROV-5 (A), M64/1 200ROV-7 (B), M64/1 209GTV-a (C), M64/1 209GTV-b (D), M64/1 213GTV (E), M64/1 214GTV (F), M68/1 39ROV-1 (G), M68/1 39ROV-7A (H), M68/1 41ROV-1 (I), and M78/2 335ROV-7 (J).

positive correlation between the  $\delta^{18}\text{O}$  and the silica content is indicated by the measured data (Tables 4 and 5). According to Yapp (1987), the O isotope fractionation in water of natural samples consisting mainly of siliceous iron oxides can be calculated by considering both, the fractionation of goethite-water and amorphous silica-water. A mean value of 11.6 wt.%  $\text{SiO}_2$  and 60.2 wt.%  $\text{Fe}_2\text{O}_3$ , calculated from the data in Table 4, is used to estimate the ratio of siliceous oxygen to iron bound oxygen ( $\sim 1/4$ ). Assuming that iron- and silica-bound oxygen is the only oxygen fraction in the precipitated samples, Eq. (1) then defines the isotope value of the hydrothermal precipitate. However, this is a rough assumption, considering other XRD-amorphous compounds in the order of some

wt.% (Table 1). The  $\delta^{18}\text{O}$  values in Eq. (1) can be calculated for  $\text{SiO}_2$  by Kita et al. (1985) and for  $\text{FeOOH}$  by Yapp (2007).

$$\delta^{18}\text{O}_{\text{mix}} = 0.2 \times \delta^{18}\text{O}_{\text{SiO}_2} + 0.8 \times \delta^{18}\text{O}_{\text{FeOOH}} \quad (1)$$

For  $\delta^{18}\text{O}_{\text{H}_2\text{O}} \sim 0\text{‰}$ , and bottom water temperatures of 3.6 and 20 °C, a  $\delta^{18}\text{O}_{\text{mix}}$  of 16.3 and 12.7‰, respectively, can be calculated.

#### 4.3. Microbiology associated with the deposits

SEM observations revealed that the majority of the studied yellow to red samples from the Lilliput hydrothermal field are composed of

**Table 3**  
85 K Mössbauer parameters<sup>a</sup> of hydrothermal precipitates from the Lilliput hydrothermal field (Mid-Atlantic Ridge).

Sample #	Doublet			Sextet				Mineralogy (Mössbauer data)
	A (%)	$\delta$ (mm/s)	$\Delta$ (mm/s)	A (%)	$\delta$ (mm/s)	B (T)	$\Delta$ (mm/s)	
M64/1 200ROV-5	100	0.45	0.82					Ferrihydrite
M64/1 200ROV-7	100	0.45	0.80					Ferrihydrite
M64/1 209GTV-a	100	0.46	0.80					Ferrihydrite
M64/1 209GTV-b	49.3	0.46	0.79	50.7	0.51	43.9	−0.23	Goethite, ferrihydrite
M64/1 213GTV	48.7	0.46	0.78	51.3	0.49	42.7	−0.24	Goethite, ferrihydrite
M64/1 214GTV	60.2	0.45	0.79	39.8	0.49	42.1	−0.21	Goethite, ferrihydrite
M68/1 39ROV-1	100	0.45	0.81					Ferrihydrite
M68/1 39ROV-7A	72.8	0.45	0.76	27.2	0.51	41.9	−0.22	Ferrihydrite, goethite
M68/1 41ROV-1	395	0.46	0.80	60.5	0.51	45.2	−0.21	Goethite, ferrihydrite
M78/2 335ROV-7	100	0.46	0.85					Ferrihydrite

<sup>a</sup> A = line area,  $\delta$  = isomer shift, B = hyperfine magnetic field,  $\Delta$  = quadrupole splitting.

dense, bacteria-like structures [varying from spherical (~1–2  $\mu\text{m}$  across) to spider net-like (Fig. 3C) and net-like (Fig. 3D)] encrusted with Fe–Si-oxyhydroxides (EDS data). Similar structures have also been documented in other oxyhydroxides (Inskeep et al., 2004; Santelli et al., 2008). The networks (Fig. 3C) bear a resemblance to those formed by organisms comprising biofilms (Baum et al., 2009). The bacteria-like filaments are <1  $\mu\text{m}$  in diameter and ~10  $\mu\text{m}$  in length. The thin, black films on the surfaces of the yellow to red deposits are also composed of thread-like bacterial structures, but are encrusted with Fe-sulfides (Fig. 3E, F). However, their dimensions (diameter of 10–20  $\mu\text{m}$ , length of ~100  $\mu\text{m}$ ) differ markedly from those of the Fe–Si-oxyhydroxide-encrusted bacterial filaments. Fe–Si-oxyhydroxide mat material collected from the vicinity of the mussel patch (Fig. 2E, F) encompassed various shapes likely associated with mineralized microbial surfaces as has been recognized for distinct Fe<sup>2+</sup>-oxidizers (Fig. 10). The observed structures included non-helical filaments (Fig. 10A, B) resembling those known from the *Mariprofundus ferrooxydans* strain PV-1 (Emerson et al., 2007), helical stalks (Fig. 10A, C) likewise found in *Galionella ferruginea* (Hallbeck and Pedersen, 1991), some randomly coiled and irregular twisted branching forms (Fig. 10D, E) and some sheathed shapes (Fig. 10F), which could be associated with *Leptothrix ochracea* (Emerson and Revsbech, 1994).

## 5. Discussion

### 5.1. Geochemistry of Lilliput Fe–Si-oxyhydroxide deposits

Low-temperature diffuse venting observed and sampled by ROV are direct evidence that the yellow to red deposits of the Lilliput field are hydrothermal precipitates. The hydrothermal origin of these deposits is supported by their chemical composition: they are rich in Fe (and Si) and have very low concentrations of Al (and Ti) and transition elements, which results in extremely low Al/(Al + Fe + Mn) ratios (<<0.4; Bonatti, 1981) and a plot at the Fe-rich corner of the Mn–Fe–(Co + Ni + Cu)  $\times$  10 ternary diagram of seafloor Fe–Mn deposits (Fig. 11). High Fe and Si concentrations correlate with significantly

increased (relative to the ambient seawater) dissolved Fe and Si concentrations in the vent fluids (Haase et al., 2009). In a comprehensive study of hydrothermal Fe–Si-oxyhydroxides from the south Pacific intraplate volcanoes and East Pacific Rise Hekinian et al. (1993) divided them into four groups based on their geologic setting, morphology and composition. According to this classification all the studied Lilliput deposits belong to type 1 (Hekinian et al., 1993): Fe–Si-oxyhydroxides forming chimneys, mounds and flat-lying deposits, depleted in trace- and rare earth elements with Fe = 25–50 wt.% and Si = 4–10 wt.%. Chondrite-normalized REE distribution patterns of Lilliput Fe–Si-oxyhydroxide deposits [with both negative Ce anomalies (Ce/Ce\* < 1) and negative Eu anomalies (Eu/Eu\* < 1); Fig. 7, Table 4] are comparable to that of the Atlantic deep seawater. These patterns and the very low total REE abundance indicate a low-temperature hydrothermal origin (Hekinian et al., 1993; Usui et al., 1997) of the Fe–Si-oxyhydroxides. Most probably they have precipitated from a fluid composed primarily of ambient seawater with little proportion of hydrothermal fluid. This conclusion is supported by the measured venting fluid temperatures (<20  $^{\circ}\text{C}$ ) and Mg concentrations in the vent fluids (slightly lower than those in seawater; Haase et al., 2009).

The low-temperature formation (~3.6–20  $^{\circ}\text{C}$ ) is also supported by the  $\delta^{18}\text{O}$ -values measured in selected Fe–Si-oxyhydroxides (Table 5). The measured data (12.3–19.4‰) is comparable to the calculated data (12.7–16.3‰), considering published isotope equilibrium equations for goethite and amorphous silica (Kita et al., 1985; Yapp, 2007). Slightly more positive measured  $\delta^{18}\text{O}$ -values (i.e., 19.4‰) of the Fe–Si-oxyhydroxide mixture in sample M78/2 335ROV-7 can either reflect the higher silica content of this sample when compared to the calculated mean value used in Eq. (1) (see 4.) or a higher contribution of more positive hydrothermal fluid. Furthermore, the calculated formation temperature range (3.6–20  $^{\circ}\text{C}$ ) should be used only as an indicator, as precise determination of the original  $\delta^{18}\text{O}$ -value of natural Fe–Si-oxyhydroxides is hard to reach and also published isotope fractionation equations for FeOOH differ significantly from each other (see discussion in Yapp, 1987, 2007).

Precipitation of Fe–Si-oxyhydroxides from a fluid composed primarily of seawater is also supported by the Sr systematics of the hydrothermal precipitates. Fe–Si-oxyhydroxides <sup>87</sup>Sr/<sup>86</sup>Sr ratios are overall swamped by seawater Sr, so any contribution from the underlying basalts is negligible (Fig. 8). Nd, on the other hand, shows mixed isotopic signature indicating derivation of Nd from seawater/sediments and local basalts (Fig. 8). As can be seen (Fig. 8), the oxyhydroxides form a trend from values similar to Atlantic sediments and/or Southern Component Water (SCW) to higher epsilon values, suggesting some basaltic influence on the Nd isotopic systematics. Overall, the Sr–Nd isotopic systematics of the Lilliput Fe–Si-oxyhydroxide deposits are very similar to the isotopic compositions observed in 12°50'N MAR low-temperature precipitates, where Sr is also swamped by seawater, and Nd shows mixing relationships between

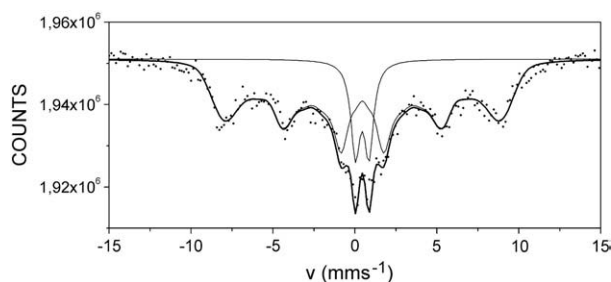


**Fig. 6.** 25 K Mössbauer spectrum of sample M68/1 41ROV-1.

**Table 4**  
Chemical composition (XRF and ICP-MS) of hydrothermal precipitates from the Lilliput hydrothermal field (Mid-Atlantic Ridge).

Sample #	SiO <sub>2</sub> (wt.%)	Al <sub>2</sub> O <sub>3</sub>	Fe <sub>2</sub> O <sub>3</sub>	Cr <sub>2</sub> O <sub>3</sub>	MnO	TiO <sub>2</sub>	P <sub>2</sub> O <sub>5</sub>	CaO	MgO	K <sub>2</sub> O	Na <sub>2</sub> O	SO <sub>3</sub>	L.O.I.	Total	Al/(Al + Fe + Mn)	Fe/Mn	Li (ppm)	Sc	V
M64/1 200ROV-5	13.11	0.11	58.44	0.003	0.374	0.02	1.506	2.11	1.32	0.25	5.17	0.65	16.63	99.69	0.001	141	4.46	<1.51	179
M64/1 200ROV-7	10.87	<0.02	60.78	0.009	0.722	0.02	0.799	1.85	1.38	0.20	3.80	0.58	18.69	99.70	-	76	6.52	<1.51	188
M64/1 209GTV-a	8.92	0.04	67.45	0.003	0.599	0.02	0.240	1.56	1.09	0.14	2.51	0.07	16.99	99.63	0.001	102	7.22	<1.51	11.4
M64/1 209GTV-b	11.04	0.08	66.59	0.005	0.184	0.02	0.410	1.29	0.97	0.14	2.55	0.08	16.36	99.72	0.001	327	4.39	<1.51	51.5
M64/1 213GTV	13.28	0.38	61.23	0.007	0.059	0.02	0.996	0.64	0.77	0.18	5.85	0.11	16.29	99.81	0.005	937	3.17	<1.51	74.4
M64/1 213GTV-3	-	-	-	-	-	-	-	-	-	-	-	-	-	-	-	-	6.99	<1.51	18.2
M64/1 214GTV	11.67	0.27	63.92	0.002	0.109	0.01	0.951	1.07	0.99	0.14	2.72	0.23	17.69	99.77	0.003	530	5.81	<1.51	71.4
M64/1 214GTV-3	-	-	-	-	-	-	-	-	-	-	-	-	-	-	-	-	8.47	<1.51	8.30
M68/1 39ROV-1	10.26	<0.02	60.27	0.005	0.026	0.02	0.231	1.00	1.09	0.25	5.42	0.53	20.68	99.78	-	2093	2.05	<1.51	45.1
M68/1 39ROV-7A	9.49	0.05	63.82	0.005	0.409	0.02	0.563	1.65	1.18	0.18	4.18	0.49	17.70	99.74	0.001	141	5.85	<1.51	63.9
M68/1 41ROV-1	10.07	0.37	53.79	0.003	0.034	0.02	0.804	0.87	0.86	0.19	4.09	7.11	21.57	99.78	0.005	1429	4.02	<1.51	126
M78/2 335ROV-7	16.32	<0.02	57.46	0.001	0.025	0.02	0.450	1.63	1.14	0.29	3.98	0.51	17.98	99.81	-	2076	5.36	<1.51	24.8

<sup>a</sup> Ce/Ce\* = 2Ce<sub>N</sub>/(La<sub>N</sub> + Pr<sub>N</sub>).

<sup>b</sup> Eu/Eu\* = 2Eu<sub>N</sub>/(Sm<sub>N</sub> + Gd<sub>N</sub>).

**Table 4** (continued)

Sample #	Co (ppm)	Ni	Cu	Zn	Rb	Sr	Y	Zr	Nb	Mo	Cd	Sn	Sb	Cs	Ba	La	Ce	Pr	Nd	Sm
M64/1 200ROV-5	3.52	2.76	36.6	138	0.87	413	6.90	3.03	0.160	75.7	0.748	<1.77	2.00	<0.09	53.5	2.97	2.75	0.521	2.30	0.475
M64/1 200ROV-7	48.8	14.5	13.5	18.0	0.83	552	3.48	<2.13	0.052	94.8	0.375	<1.77	3.30	<0.09	52.9	0.818	0.262	0.093	0.409	0.090
M64/1 209GTV-a	9.63	4.43	377	<6.23	0.46	462	2.81	<2.13	0.009	104	0.352	<1.77	3.59	<0.09	36.5	0.824	0.292	0.028	0.109	0.021
M64/1 209GTV-b	7.36	1.79	175	<6.23	0.49	347	2.86	<2.13	0.026	77.9	0.197	<1.77	2.22	<0.09	28.4	1.07	0.701	0.095	0.422	0.071
M64/1 213GTV	1.06	1.01	10.7	10.5	0.59	174	15.1	<2.13	0.075	144	0.154	<1.77	2.70	<0.09	14.7	4.97	7.13	0.960	4.40	0.870
M64/1 213GTV-3	6.22	4.26	12.2	12.4	1.39	10.9	1.05	<2.13	0.198	213	0.345	<1.77	1.53	0.45	3.78	0.400	0.927	0.143	0.670	0.175
M64/1 214GTV	1.32	<0.91	17.9	7.22	0.58	231	9.07	<2.13	0.042	117	0.163	<1.77	3.33	<0.09	20.7	4.17	3.34	0.366	1.53	0.247
M64/1 214GTV-3	1.48	2.99	10.7	6.51	0.74	8.24	0.74	<2.13	0.030	171	0.283	<1.77	1.35	0.34	1.80	0.281	0.594	0.089	0.397	0.099
M68/1 39ROV-1	0.45	1.33	58.5	22.4	1.09	271	7.52	<2.13	0.053	84.7	0.073	<1.77	0.41	<0.09	31.7	4.52	3.54	0.597	2.43	0.461
M68/1 39ROV-7A	14.3	4.04	8.38	37.7	0.60	479	1.21	<2.13	0.019	83.6	0.313	<1.77	4.31	<0.09	39.9	0.185	0.089	0.027	0.127	0.035
M68/1 41ROV-1	0.89	1.47	13.8	7.84	0.94	165	11.4	2.45	0.173	140	0.137	<1.77	3.06	<0.09	23.1	4.15	4.49	0.595	2.70	0.544
M78/2 335ROV-7	<0.19	<0.91	8.12	<6.23	0.99	455	4.40	<2.13	0.042	33.9	0.115	<1.77	0.67	<0.09	25.3	3.30	3.55	0.505	2.23	0.434

**Table 4** (continued)

Sample #	Eu (ppm)	Gd	Tb	Dy	Ho	Er	Tm	Yb	Lu	ΣREE	(Ce/Ce*) <sup>a</sup>	(Eu/Eu*) <sup>b</sup>	La <sub>N</sub> /Lu <sub>N</sub>	Hf	Ta	W	Tl	Pb	Th	U
M64/1 200ROV-5	0.142	0.690	0.107	0.699	0.169	0.509	0.069	0.447	0.077	11.9	0.50	0.76	4.10	<0.06	<0.46	0.38	0.45	5.93	<0.07	13.2
M64/1 200ROV-7	0.027	0.133	0.022	0.172	0.047	0.157	0.025	0.159	0.028	2.44	0.19	0.76	3.12	<0.06	<0.46	0.65	0.97	<0.32	<0.07	5.70
M64/1 209GTV-a	0.006	0.060	0.009	0.070	0.026	0.087	0.011	0.069	0.014	1.63	0.25	0.49	6.37	<0.06	<0.46	0.35	0.55	<0.32	<0.07	12.2
M64/1 209GTV-b	0.020	0.144	0.024	0.166	0.047	0.151	0.021	0.131	0.024	3.09	0.41	0.60	4.87	<0.06	<0.46	0.37	0.10	<0.32	<0.07	8.53
M64/1 213GTV	0.295	1.61	0.250	1.66	0.413	1.23	0.168	1.05	0.184	25.2	0.75	0.75	2.89	<0.06	<0.46	0.82	0.05	<0.32	<0.07	18.7
M64/1 213GTV-3	0.056	0.218	0.038	0.247	0.054	0.167	0.024	0.166	0.027	3.31	0.95	0.87	1.57	<0.06	<0.46	<0.29	0.17	2.98	<0.07	1.78
M64/1 214GTV	0.086	0.594	0.086	0.603	0.171	0.524	0.064	0.391	0.072	12.2	0.51	0.66	6.21	<0.06	<0.46	0.62	0.11	<0.32	<0.07	15.3
M64/1 214GTV-3	0.033	0.159	0.024	0.163	0.038	0.109	0.017	0.109	0.018	2.13	0.91	0.81	1.63	<0.06	<0.46	<0.29	0.19	<0.32	<0.07	1.16
M68/1 39ROV-1	0.140	0.749	0.112	0.725	0.161	0.456	0.059	0.358	0.056	14.4	0.46	0.72	8.73	<0.06	<0.46	<0.29	0.04	<0.32	<0.07	5.16
M68/1 39ROV-7A	0.011	0.042	0.007	0.051	0.014	0.047	0.008	0.051	0.010	0.71	0.27	0.87	2.07	<0.06	<0.46	0.68	0.51	<0.32	<0.07	10.5
M68/1 41ROV-1	0.175	0.954	0.147	0.993	0.246	0.739	0.099	0.631	0.110	16.6	0.62	0.74	4.04	<0.06	<0.46	0.81	0.14	0.56	<0.07	11.2
M78/2 335ROV-7	0.129	0.675	0.097	0.603	0.135	0.384	0.051	0.308	0.050	12.4	0.60	0.73	7.08	<0.06	<0.46	<0.29	0.02	<0.32	<0.07	3.99

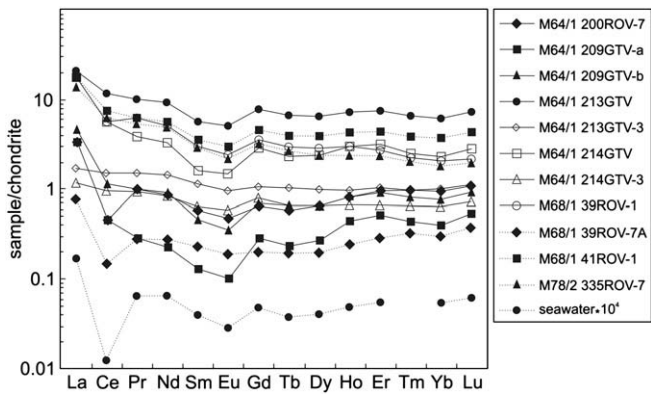


Fig. 7. REE distribution patterns of the studied Lilliput hydrothermal deposits. Seawater = Atlantic deep seawater (Douville et al., 1999).

seawater/sediments and local basalts (Dekov et al., submitted for publication). The only sample that shows predominantly basalt-derived Sr and Nd is M64/1 200ROV-7 (Table 5; Figs. 8, 9). Dekov et al. (submitted for publication) showed that Fe-oxhydroxides formed after primary Fe-sulfides can preserve the protolith isotopic signature. Therefore, it is possible that the precursor of M64/1 200ROV-7 was a primary, high-temperature Fe-sulfide that was eventually altered to ferrihydrite. However, the Pb isotopic composition of M64/1 200ROV-7 is completely swamped by sediment-derived Pb (Fig. 9) and as this sample represents a red cover on the top of pillow lava, it is quite possible that some basalt shards contributed to the observed Sr–Nd isotopic compositions, without having much effect on the Pb isotopes.

The majority of the Fe–Si-oxhydroxide samples plot mainly in the Atlantic sediment field on the Pb–Pb isotopic diagram with exception of two samples, M64/1 200ROV-5 and M68/1 39ROV-1, which plot away from the sediment field (Fig. 9; Table 5). The Pb isotopic systematics of sample M68/1 39ROV-1 can be explained by mixing of Pb from basaltic and seawater/sedimentary sources, similar to Nd as described above. Sample M64/1 200ROV-5, however, has very different Pb isotopic compositions from the analyzed local MORB and possible seawater/sedimentary sources, but is similar to the observed Pb isotopic compositions of regional Atlantic MORB samples (Fig. 9). This sample was collected slightly to the south of the majority of the Lilliput samples (Fig. 1),

Table 5  
Pb, Sr, Nd, and O isotope data for samples from the Lilliput hydrothermal field (Mid-Atlantic Ridge).

Sample #	$^{206}\text{Pb}/^{204}\text{Pb}$	$^{207}\text{Pb}/^{204}\text{Pb}$	$^{208}\text{Pb}/^{204}\text{Pb}$	$^{87}\text{Sr}/^{86}\text{Sr}$	Error	$^{143}\text{Nd}/^{144}\text{Nd}$	Error	$\epsilon\text{Nd}$	$\delta^{18}\text{O}$ (‰ SMOW)
<i>Fe–Si-oxhydroxides</i>									
M64/1 200ROV-5	17.771	15.446	37.286	0.70916	0.000015	0.512488	0.0000099	–2.9	16.2
M64/1 200ROV-7	18.621	15.629	38.540	0.70312	0.000011	0.513004	0.0000071	7.1	15.9
M64/1 209GTV-a				0.70916					
M64/1 209GTV-b	18.810	15.625	38.706	0.70911	0.000012	0.512374	0.000013	–5.2	13.0
M64/1 213GTV	18.604	15.637	38.495	0.70916	0.000013	0.512838	0.0000077	3.9	
M64/1 214GTV	18.689	15.628	38.577	0.70915	0.000011	0.512723	0.0000062	1.7	
M64/1 214GTV-3				0.70912	0.000014				
M68/1 39ROV-1	18.356	15.570	38.107	0.70917	0.000010	0.512409	0.0000051	–4.5	15.2
M68/1 39ROV-7A	18.842	15.618	38.682	0.70917	0.000010	0.512206	0.000022	–8.4	15.9
M68/1 41ROV-1	18.690	15.631	38.582	0.70917	0.000012	0.512748	0.0000072	2.2	12.3
M78/2 335ROV-7	18.512	15.625	38.377	0.70917	0.000010	0.512685	0.0000059	0.9	19.4
<i>Basalts</i>									
M64/1 194ROV-13	19.036	15.608	38.841	0.70270	0.000014	0.513033	0.0000057	7.7	
M64/1 194ROV-4	19.113	15.582	38.829	0.70274	0.000010	0.513048	0.0000071	8.0	
M64/1 200ROV-3	19.055	15.606	38.865	0.70280	0.000010	0.51306	0.0000077	8.2	
M64/1 200ROV-1	19.067	15.632	38.944						

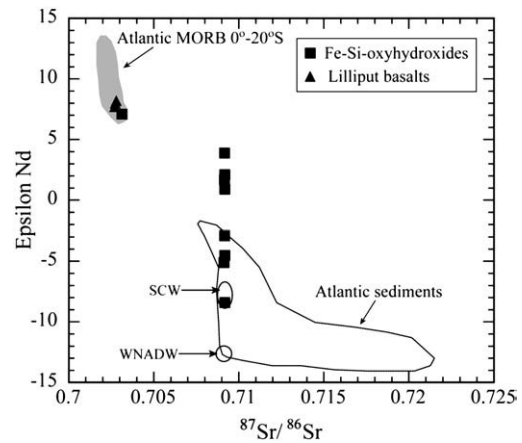


Fig. 8. Sr–Nd isotope data for Lilliput Fe–Si-oxhydroxide deposits compared to possible sources in the region. Data for Atlantic MORB 0°–20° S after Agranier et al. (2005), Atlantic sediments after Ben Othman et al. (1989), Southern Component Water (SCW) and Western North Atlantic Deep Water (WNADW) after Abouchami et al. (1999). Note that the Sr isotopic compositions of the oxhydroxides are completely swamped by seawater Sr and the Nd isotopic compositions form a trend extending from Atlantic sediments/SCW to more radiogenic values, indicating contribution from local basalts, for more discussion see the text.

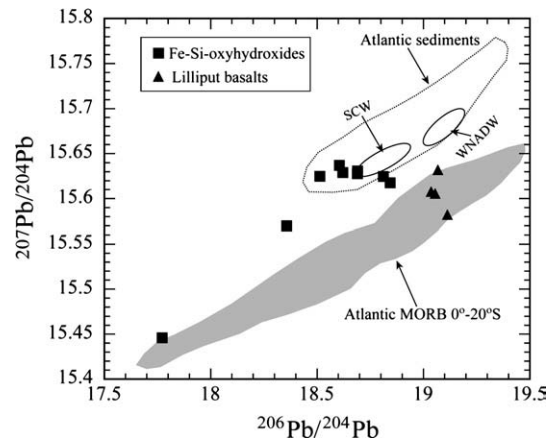
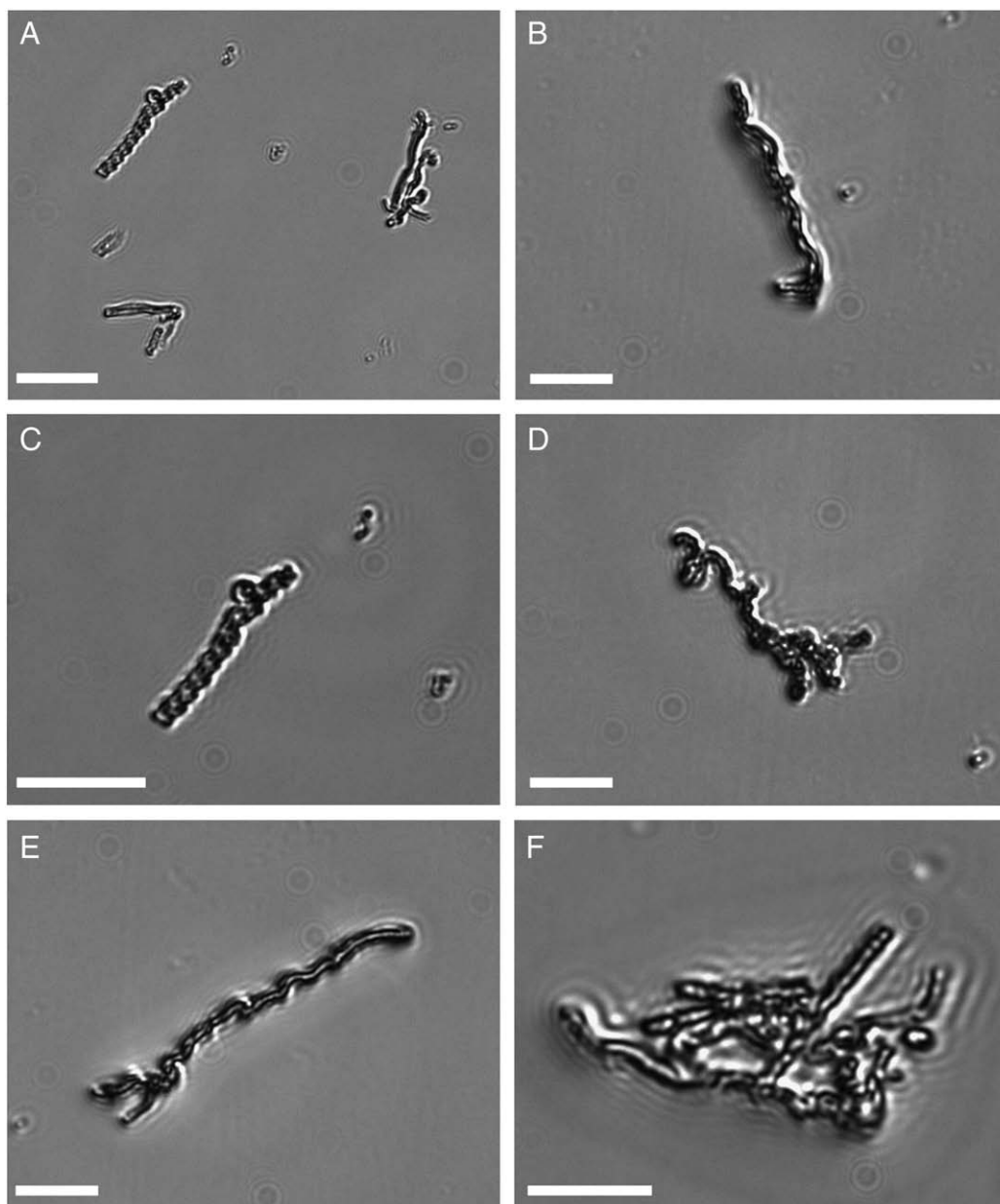


Fig. 9. Pb isotope data for Lilliput Fe–Si-oxhydroxide deposits compared to possible sources in the region. Data for Atlantic MORB 0°–20° S after Agranier et al. (2005), Atlantic sediments after Ben Othman et al. (1989), Southern Component Water (SCW) and Western North Atlantic Deep Water (WNADW) after Abouchami et al. (1999). Note that majority of the samples plot within the Atlantic sediment field suggesting Pb derivation from the latter, for more discussion see the text.



**Fig. 10.** Transmitted light microscopy of white fluffy and reddish mat material covering Fe–Si-oxyhydroxides (Fig. 2E, F) collected from site M78/2 319ROV-5 at the Lilliput hydrothermal field. Different microbial-like structures in these samples resemble those produced by known  $\text{Fe}^{2+}$ -oxidizers. (A, B) non-helical filaments resembling those of *Mariprofundus ferrooxydans* strain PV-1 (Emerson et al., 2007); (C) helical stalks similar to those found around *Galionella ferruginea* (Hallbeck and Pedersen, 1991); (D, E) randomly coiled and irregularly twisted branching forms; (F) sheathed shapes that could be associated with *Leptothrix ochracea* (Emerson and Revsbech, 1994). Scale bars equal to 10  $\mu\text{m}$ .

therefore it is possible that it formed over primary Fe-sulfides (cf. Dekov et al., submitted for publication) and reflects heterogeneity in the Pb isotopic compositions of the local MORB. The observed overall Pb isotopic similarity between the majority of the Lilliput hydrothermal deposits and Atlantic sediments suggest Pb is controlled by the latter. In addition, as can be seen from the Fig. 9, few samples also show similarity to the SCW. Kamenov et al. (2009) showed that Pb isotope systematics in low-temperature hydrothermal precipitates are predominantly controlled by Pb scavenged from the local seawater, which itself can be controlled by regional atmospheric input. Most probably significant part of the seawater Pb available for scavenging by precipitating Fe–Si-oxyhydroxides in the Lilliput area is released from the sedimentary input in this part of the Atlantic Ocean, evident in the isotopic similarity between the former and the latter (Fig. 9).

## 5.2. Mechanisms of Fe precipitation at Lilliput hydrothermal field

Two types of Fe-deposits occur at the Lilliput hydrothermal field: Fe–Si-oxyhydroxides and Fe-sulfides. The Fe–Si-oxyhydroxide precipitates comprise the majority of the Lilliput hydrothermal deposits, while the Fe-sulfides constitute roughly 1% of all the Fe formations. In both types of deposits we observed pervasive microbial structures encrusted by Fe-containing precipitates. There are three alternative ways of how these deposits formed. Precipitation can be related to: (i) microbially mediated processes; (ii) abiogenic processes (microbes are simply embedded in the precipitate matrix); or (iii) a combination of both abiogenic and biogenic processes.

It is well known that the microbial mats are complex ecosystems, which inhabit a wide range of environments (caves, salt marshes, lagoons, cold seeps, seafloor hydrothermal vents, etc.) (Franks and

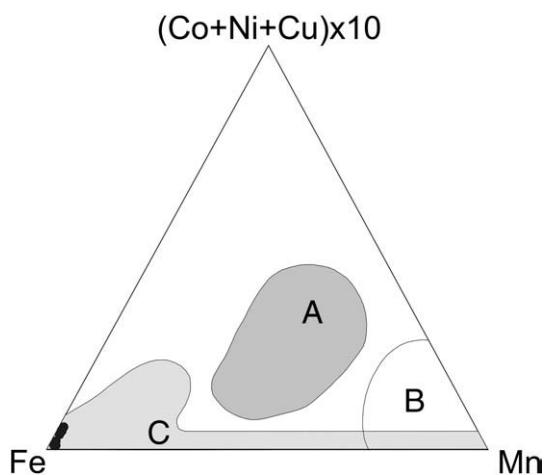


Fig. 11. Mn-Fe-(Co+Ni+Cu)x10 ternary diagram of seafloor Fe-Mn deposits (after Bonatti et al., 1972): A = hydrogenetic, B = diagenetic, C = hydrothermal. Closed circles = Lilliput hydrothermal deposits.

Stolz, 2009). Submarine hydrothermal sites provide habitats for various microbial communities and filamentous microorganisms are widely observed at them (Jannasch and Wirsén, 1981; Baross and Deming, 1985; Karl, 1995; Juniper et al., 1998; Cowen et al., 1999; Glazer and Rouxel, 2009; Davis et al., 2009; Sudek et al., 2009; Takai et al., 2009).

The low-temperature hydrothermal fluids of the Lilliput vent field emanate considerable amounts of reduced  $\text{Fe}^{2+}$  (Perner et al., 2007; Haase et al., 2009). When  $\text{Fe}^{2+}$  comes into contact with the oxygenated ambient seawater it is oxidized to  $\text{Fe}^{3+}$ , which is then hydrolyzed and precipitated to form poorly ordered Fe-oxyhydroxides, like 2-line ferrihydrite or goethite (Schwertmann and Murad, 1983; Jambor and Dutrizac, 1998). The rate controlling mechanism for the Fe-bearing mineral formation is the oxidation of  $\text{Fe}^{2+}$ , rather than the rapid  $\text{Fe}^{3+}$  hydrolysis and precipitation (see references in Kasama and Murakami, 2001). However, microbially mediated  $\text{Fe}^{2+}$  oxidation can proceed faster than abiogenic  $\text{Fe}^{2+}$  oxidation (Kasama and Murakami, 2001). Indeed, neutrophilic  $\text{Fe}^{2+}$ -oxidizers have been detected in several hydrothermally influenced environments and their importance for Fe-oxyhydroxide deposition has been subjected to particular attention (e.g., Boyd and Scott, 2001; Emerson and Moyer, 2002; Kennedy et al., 2003b; Hodges and Olson, 2009; Toner et al., 2009).

#### 5.2.1. Fe-Si-oxyhydroxide formation

Microstructures (spherical and web-like) similar to those we observed in the Lilliput Fe-Si-oxyhydroxides (Fig. 3C, D) have previously been documented from Fe-rich environments, where microbially mediated  $\text{Fe}^{2+}$ -oxidation has been suggested as the dominant metabolism and where  $\text{Fe}^{3+}$ -mineral deposition has been linked to microbial activity (Inskeep et al., 2004; Santelli et al., 2008). Additionally, in the red Fe-oxyhydroxide mat material we identified morphological shapes, which strongly resemble those produced by distinct  $\text{Fe}^{2+}$ -oxidizers (Fig. 10). The non-helical filaments bear similarity to those known from the *M. ferrooxydans* strain PV-1 (Emerson et al., 2007). The helical stalks are comparable to those produced by *G. ferruginea* (Hallbeck and Pedersen, 1991). Some sheathed shapes appear similar to those associated with *Leptothrix ochracea* (Emerson and Revsbech, 1994). These types of structures as well as other shapes, which have not been classified to date, but which are present in our samples too (Fig. 10) have been repetitively identified in distinct hydrothermally influenced environments, where Fe-oxyhydroxides were present (e.g., Boyd and Scott, 2001; Edwards et al., 2003b; Kennedy et al., 2003a).

Bacteria can secrete extracellular polymer substrates (EPS) for attachment and protection from environmental conditions, thereby forming biofilms. These EPS act as reactive geochemical surfaces for poorly ordered Fe-Si-oxyhydroxides (Fortin et al., 1998; Ueshima and Tazaki, 2001; Phoenix et al., 2003; Yee et al., 2003; Lalonde et al., 2005). The precipitation of Fe-oxyhydroxides is supposed to be initiated by direct binding of the dissolved  $\text{Fe}^{2+}$  from the vent fluids to reactive sites (e.g.,  $\text{COOH}^-$ ,  $\text{PO}_4^{3-}$ , and  $\text{OH}^-$  groups) present within the bacterial cell wall and the exopolymers (Fortin et al., 1998), since metal ions have been shown to have a high affinity for bacterial cell wall components (Fein et al., 1997). Dissolved silicate anions ( $\text{SiO}_4^{4-}$ ) can adhere to positively charged  $\text{R-NH}_3^+$  groups present within the cell wall and initiate silica nucleation.  $\text{SiO}_4^{4-}$  anions can also adhere to negatively charged binding sites ( $\text{COOH}^-$  and  $\text{PO}_4^{3-}$  groups) through a metal cation bridging, as a result of electrostatic interactions (Urrutia and Beveridge, 1994). The presence of  $\text{Fe}^{3+}$ -coated bacteria significantly increases silica sorption/precipitation rates, and the extent of Si sorption/precipitation increases with increasing  $\text{Fe}^{3+}$  concentrations, i.e., a metal cation (Fe), is necessary for the sorption/precipitation of Si onto bacterial surfaces (Urrutia and Beveridge, 1994).

It has been pointed out before that most likely a great deal of  $\text{Fe}^{2+}$ -oxidizers are not being recognized when using culture independent methods because of their close phylogenetic association with certain heterotrophic species (cf. Edwards et al., 2003a). Hence, despite the lack of genetic evidence for the presence of typical  $\text{Fe}^{2+}$ -oxidizers in the Lilliput hydrothermal emissions (Perner et al., 2007), the pervasive microbial structures encrusted by Fe-Si-oxyhydroxides (SEM-EDS) (Figs. 3C, D; and 10) resemble textures known to be produced by  $\text{Fe}^{2+}$ -oxidizers. We therefore argue that while some of the microbes detected in the Lilliput oxyhydroxide deposits are surely just embedded in the Fe-Si-precipitates, a considerable part encrusted by Fe-Si-oxyhydroxides appears to be responsible for the Fe-Si-oxyhydroxide precipitation at the Lilliput field.

#### 5.2.2. Fe-sulfide (black films) formation

A very negligible part (by volume, ~1%) of the Lilliput deposits is the black films scarcely staining the (internal?) surfaces of the oxyhydroxide chimneys. Their sulfide composition (Tables 1 and 4) suggests depositional environment contrasting to that of the bulk Fe-Si-oxyhydroxide matrix. These pyrite-marcasite stains have obviously formed in a reducing microenvironment. We see two possible genetic scenarios for their formation: (1) biological precipitation by sulfate-reducing bacteria; and (2) dissolution of primary Fe-oxyhydroxides and re-precipitation of pyrite-marcasite.

The first mechanism is very similar to  $\text{FeS}_2$  deposition in anoxic sediments (cf. Konhauser, 1998) where the  $\text{FeS}_2$  precipitation is associated with the activity of sulfate-reducing bacteria, which couple the oxidation of organic compounds to sulfate reduction thereby producing sulfide. The released sulfide can then react with Fe-oxyhydroxides whereby  $\text{FeS}$  and  $\text{S}^0$  are formed. To transform  $\text{FeS}$  to pyrite oxidized sulfur species act as oxidants. In fluids containing both high concentrations of  $\text{Fe}^{2+}$  and  $\text{SO}_4^{2-}$ , biological pyrite fixation, which is mediated by sulfate-reducing bacteria, is possible (Bottrell and Morton, 1992). The Lilliput hydrothermal fluids contain elevated  $\text{Fe}^{2+}$  concentrations and likely high amounts of  $\text{SO}_4^{2-}$ . The latter is related to the fact that a high proportion of ambient seawater is admixed to the vent fluids (Perner et al., 2007). Whatever the sulfur source is (derived from hydrothermal fluids or sulfate-reducing bacterial activity), biological pyrite precipitation in the Lilliput vents is a potential mechanism for the black  $\text{FeS}_2$  films staining the (internal?) walls of the chimney channels.

We cannot rule out the second scenario of black film formation: dissolution of primary Fe-oxyhydroxides and re-precipitation of pyrite-marcasite in a reduced microenvironment. The  $\text{CH}_4$  concentrations in the Lilliput vent fluids (or the organic substances of the decayed bacterial cells from the internal parts of the chimneys) might

indeed be high enough to locally reduce the Fe-oxyhydroxides. The released  $\text{Fe}^{2+}$  could re-precipitated as Fe-sulfide (pyrite and marcasite) in case of sufficient  $f_5$  ( $\text{H}_2\text{S}$  concentration) in the fluid. The main geochemical consequence of this dissolution/re-precipitation process is modification of the trace- and rare earth element signature of the ultimate phase (sulfide) relative to that of the precursor (Fe-oxyhydroxide) (see 4.): gain and loss of elements from/to the fluid. These processes are most expressive in the REE distribution patterns of the pairs yellow to red Fe–Si-oxyhydroxide precipitates—black sulfide films (Fig. 7). The proposed mechanism of dissolution/re-precipitation has led to a general depletion in REE of the ultimate phase (black films) and erasure of the Ce and Eu anomalies of the precursor (oxyhydroxides).

## 6. Conclusions

Our investigations of the low-temperature hydrothermal deposits of the Lilliput field do not support the assumption that a thickened oceanic crust fuels hydrothermal systems different from their thin-crust counterparts. Lilliput hydrothermal deposits do not differ principally in composition, structure and morphology from the other low-temperature hydrothermal deposits of mid-ocean ridges and hotspot volcanoes. They are composed of Fe-oxyhydroxides rich in silica, goethite and ferrihydrite, have very low concentrations of a number of micro- and rare earth elements and show REE distribution patterns with both negative Ce and negative Eu anomalies, and a slight enrichment in LREE relative to HREE. The Fe speciation ( $\text{Fe}^{2+}$  and  $\text{Fe}^{3+}$ ), precipitation (sulfides and oxyhydroxides), and preservation at the Lilliput hydrothermal field appears to be mainly organically-controlled (organic compounds and live microbes). (Bio)minerals precipitate at low-temperature conditions ( $\delta^{18}\text{O}$ ) and the observed Sr–Nd–Pb isotopic variations suggest that the Fe–Si-oxyhydroxides scavenged metals predominantly from the ambient seawater.

The MAR over the Ascension hotspot resembles the GSC (over the Galápagos hotspot), Reykjanes Ridge (over the Iceland hotspot) and Southeast Indian Ridge (over the Amsterdam–St. Paul hotspot) as location of reduced hydrothermal venting. On the basis of our studies of the Lilliput hydrothermal field we may infer that the low-temperature, diffuse venting seems to be the most important cooling agent at the hotspot-affected ridges. We are not able to estimate if the composition and extent of a seafloor hydrothermal deposit is a function of the crust thickness just on the basis of the few studies of seafloor hydrothermal deposits on thickened crust. Understanding these variables of the hydrothermal deposits at spreading centers with different crust thickness is particularly important for the global picture of transfer of heat and matter from the lithosphere to the ocean.

## Acknowledgements

We acknowledge the financial support from the Alexander von Humboldt Foundation (Resumption of the Research Fellowship grant) to V.M. Dekov and from the Hungarian Science Foundation (#OTKA K 68135) to E. Kuzmann. Samples were collected within the framework of the German DFG Priority Program 1144: “From Mantle to Ocean: Energy-, Material-, and Life-cycles at Spreading Axes”. We are grateful for the excellent work done by the ROV crews and the masters and crews of R/V *Meteor* during the respective cruises. We are indebted to J. Fein and the two anonymous reviewers for the valuable suggestions, which improved this paper. This is SPP1144 contribution no. 54.

## References

- Abouchami, W., Galer, S.J.G., Koschinsky, A., 1999. Pb and Nd isotopes in NE Atlantic Fe–Mn crusts: proxies for trace metal paleosources and paleocean circulation. *Geochim. Cosmochim. Acta* 63, 1489–1505.
- Agranier, A., Blichert-Toft, J., Graham, D., Debaille, V., Schiano, P., Albarède, F., 2005. The spectra of isotopic heterogeneities along the mid-Atlantic Ridge. *Earth Planet. Sci. Lett.* 238, 96–109.
- Baker, E.T., Haymon, R.M., Resing, J.A., White, S.M., Walker, S.L., Macdonald, K.C., Nakamura, K., 2008. High-resolution surveys along the hot spot-affected Galápagos Spreading Center: 1. Distribution of hydrothermal activity. *Geochim. Geophys. Geosyst.* 9, Q09003. doi:10.1029/2008GC002028.
- Bao, H., Koch, P.L., 1999. Oxygen isotope fractionation in ferric oxide-water systems: low temperature synthesis. *Geochim. Cosmochim. Acta* 63, 599–613.
- Baross, J.A., Deming, J.W., 1985. The role of bacteria in the ecology of black smoker environments. *Bull. Biol. Soc. Wash.* 6, 355–371.
- Baum, M., Kainović, A., O’Keefe, T., Pandita, R., McDonald, K., Wu, S., Webster, P., 2009. Characterization of structures in biofilms formed by a *Pseudomonas fluorescens* isolated from soil. *BMC Microbiol.* 9, 103.
- Ben Othman, D., White, W.M., Patchett, J., 1989. The geochemistry of marine sediments, island arc magma genesis, and crust–mantle recycling. *Earth Planet. Sci. Lett.* 94, 1–21.
- Bonatti, E., 1981. Metal deposits in the oceanic lithosphere. In: Emiliani, C. (Ed.), *The Sea*, 7. John Wiley and Sons, N.Y., USA, pp. 639–686.
- Bonatti, E., Kraemer, T., Rydell, H., 1972. Classification and genesis of submarine iron–manganese deposits. In: Horn, D.R. (Ed.), *Ferromanganese Deposits of the Ocean Floor*. Arden House, Harriman, N.Y., USA, pp. 149–166.
- Bottrell, S., Morton, M., 1992. A reinterpretation of the genesis of the Caer Coch pyrite deposit, North Wales. *J. Geol. Soc.* 149, 581–584.
- Boyd, T., Scott, S., 2001. Microbial and hydrothermal aspects of ferric oxyhydroxides and ferrous hydroxides: the example of Franklin Seamount, Western Woodlark Basin, Papua New Guinea. *Geochim. Transact.* 2, 45–56.
- Brozna, J.M., 1986. Temporal and spatial variability of seafloor spreading processes in the northern South Atlantic. *J. Geophys. Res.* 91, 497–510.
- Bruguier, N.J., Minshull, T.A., Brozna, J.M., 2003. Morphology and tectonics of the Mid-Atlantic Ridge, 7°–12°S. *J. Geophys. Res.* 108. doi:10.1029/2001JB001172.
- Campbell, B.J., Engel, A.S., Porter, M.L., Takai, K., 2006. The versatile  $\epsilon$ -proteobacteria: key players in sulphidic habitats. *Nat. Rev. Microbiol.* 4, 458–468.
- Canadian-American Seamount Expedition, 1985. Hydrothermal vents on an axis seamount of the Juan de Fuca ridge. *Nature* 313, 212–214.
- Chen, Y.J., 2003. Influence of the Iceland mantle plume on crustal accretion at the inflated Reykjanes Ridge: magma lens and low hydrothermal activity? *J. Geophys. Res.* 108 (B11), 2524. doi:10.1029/2001JB000816.
- Clayton, R.N., Mayeda, T.K., 1963. The use of bromine pentafluoride in the extraction of oxygen from oxides and silicates for isotopic analysis. *Geochim. Cosmochim. Acta* 27, 43–52.
- Corliss, J.B., Dymond, J., Gordon, L.I., Edmond, J.M., Von Herzen, R.P., Ballard, R.D., Green, K., Williams, D., Bainbridge, A., Crane, K., Van Andell, T.H., 1979. Submarine thermal springs on the Galapagos Rift. *Science* 203, 1073–1083.
- Cornell, R.M., Schwertmann, U., 2006. The iron oxides: structure, properties, reactions, occurrences. Wiley-VCH, Weinheim, pp. 152–158.
- Cowen, J.P., Shackelford, R., McGee, D., Baker, E.T., Lam, P., Olson, E.J., 1999. Microbial biomass in the hydrothermal plumes associated with the 1998 Axial Volcano eruption. *Geophys. Res. Lett.* 26, 3637–3640.
- Davis, R.E., Stakes, D.S., Wheat, C.G., Moyer, C.L., 2009. Bacterial variability within an iron–silica–manganese-rich hydrothermal mound located off-axis at the Cleft Segment, Juan de Fuca Ridge. *Geomicrobiol. J.* 26, 570–580.
- Dekov, V., Boycheva, T., Hålenius, U., Billström, K., Kamenov, G.D., Shanks, W.C., Stummeyer, J., submitted for publication. Mineralogical and geochemical evidence for hydrothermal activity at the west wall of 12°50′N core complex (Mid-Atlantic Ridge): a new ultramafic-hosted seafloor hydrothermal deposit? *Chem. Geol.*
- DeMets, C., Gordon, R.G., Argus, D.F., Stein, S., 1994. Effect of recent revisions to the geomagnetic time scale on estimates of current plate motions. *Geophys. Res. Lett.* 21, 2191–2194.
- Dick, H.J.B., Lin, J., Schouten, H., 2003. An ultraslow-spreading class of ocean ridge. *Nature* 426, 405–412.
- Douville, E., Bienuen, P., Charlou, J.L., Donval, J.P., Fouquet, Y., Appriou, P., Gamo, T., 1999. Yttrium and the rare earth elements in fluids from various deep-sea hydrothermal systems. *Geochim. Cosmochim. Acta* 63, 627–643.
- Edwards, K.J., Bach, W., Rogers, D.R., 2003a. Geomicrobiology of the ocean crust: a role for chemoautotrophic bacteria. *Biol. Bull.* 204, 180–185.
- Edwards, K.J., McCollom, T., Konishi, H., Buseck, P.R., 2003b. Seafloor bioalteration of sulfide minerals: results from in situ incubation studies. *Geochim. Cosmochim. Acta* 67, 2843–2856.
- Elderfield, H., Schultz, A., 1996. Mid-ocean ridge hydrothermal fluxes and the chemical composition of the ocean. *Annu. Rev. Earth Planet. Sci.* 24, 191–224.
- Emerson, D., Moyer, C.L., 2002. Neutrophilic Fe-oxidizing bacteria are abundant at the Loihi Seamount hydrothermal vents and play a major role in Fe oxide deposition. *Appl. Environ. Microbiol.* 68, 3085–3093.
- Emerson, D., Revsbech, N.P., 1994. Investigation of an iron-oxidizing microbial mat community located near Aarhus, Denmark—field studies. *Appl. Environ. Microbiol.* 60, 4022–4031.
- Emerson, D., Rentz, J.A., Lilburn, T.G., Davis, R.E., Aldrich, H., Chan, C., Moyer, C.L., 2007. A novel lineage of proteobacteria involved in formation of marine Fe-oxidizing microbial mat communities. *PLoS ONE* 2, e667.
- Fein, J.B., Daughney, C.J., Yee, N., Davis, T., 1997. A chemical equilibrium model of metal adsorption onto bacterial surfaces. *Geochim. Cosmochim. Acta* 61, 3319–3328.

- Fortin, D., Ferris, F.G., Scott, S.D., 1998. Formation of Fe-silicates and Fe-oxides on bacterial surfaces in samples collected near hydrothermal vents on the Southern Explorer Ridge in the northeast Pacific Ocean. *Am. Mineral.* 83, 1399–1408.
- Franks, J., Stolz, J.F., 2009. Flat laminated microbial mat communities. *Earth Sci. Rev.* 96, 163–172.
- Garbe-Schönberg, C.-D., 1993. Simultaneous determination of thirty seven trace elements in twenty eight international rock standards by ICP-MS. *Geostandards Newsl.* 17, 81–97.
- Garbe-Schönberg, D., Jähmlich, H., Koschinsky, A., Ratmeyer, V., Westernströer, U., 2006. KIPS—a new multiport valve-based all-TEFLON fluid sampling system for ROVs: EGU Meeting, Vienna, Austria, *Geophys. Res. Abstr.*, 8, # 07032.
- German, C.R., Von Damm, K.L., 2004. Hydrothermal processes. In: Turekian, K.K., Holland, H.D. (Eds.), *Treatise on Geochemistry*, 6. In: Elderfield, H. (Ed.), *The Oceans and Marine Geochemistry*. Elsevier, Oxford, pp. 181–222.
- German, C.R., Briem, J., Chin, C., Danielson, M., Holland, S., James, R., Jónsdóttir, A., Ludford, E., Moser, C., Ólafsson, J., Palmer, M.R., Rudnicki, M.D., 1994. Hydrothermal activity on the Reykjanes Ridge: the Steinahöll vent-field at 63°06'N. *Earth Planet. Sci. Lett.* 121, 647–654.
- Glazer, B.T., Rouxel, O.J., 2009. Redox speciation and distribution within diverse iron-dominated microbial habitats at Loihi Seamount. *Geomicrobiol. J.* 26, 606–622.
- Haase, K.M., Koschinsky, A., Petersen, S., Devey, C.W., German, C., Lackschewitz, K.S., Melchert, B., Seifert, R., Borowski, C., Giere, O., Paulick, H., and M64/1, M68/1 and M78/2 Scientific Parties, 2009. Diking, young volcanism and diffuse hydrothermal activity on the southern Mid-Atlantic Ridge: the Lilliput field at 9°33'S. *Mar. Geol.* 266, 52–64.
- Hallbeck, L., Pedersen, K., 1991. Autotrophic and mixotrophic growth of *Gallionella ferruginea*. *J. Gen. Microbiol.* 137, 2657–2661.
- Hannington, M.D., de Ronde, C., Petersen, S., 2005. In: Hedenquist, J.W., Thompson, J.F.H., Goldfarb, R.J., Richards, J.P. (Eds.), *Sea-floor tectonics and submarine hydrothermal systems: Economic Geology 100th Anniversary Volume*, pp. 111–141.
- Hekinian, R., Hoffert, M., Larqué, P., Cheminée, J.L., Stoffers, P., Bideau, D., 1993. Hydrothermal Fe and Si oxyhydroxide deposits from South Pacific intraplate volcanoes and East Pacific Rise axial and off-axial regions. *Econ. Geol.* 88, 2099–2121.
- Hodges, T.W., Olson, J.B., 2009. Molecular comparison of bacterial communities within iron-containing flocculent mats associated with submarine volcanoes along the Kermadec Arc. *Appl. Environ. Microbiol.* 75, 1650–1657.
- Inskeep, W., Macur, R., Harrison, G., Bostick, B., Fendorf, S., 2004. Biomineralization of As(V)-hydrous ferric oxyhydroxide in microbial mats of an acid-sulfate-chloride geothermal spring, Yellowstone National Park. *Geochim. Cosmochim. Acta* 68, 3141–3155.
- Ito, G., Lin, J., 1995. Oceanic spreading center-hotspot interactions: constraints from along-isochron bathymetric and gravity anomalies. *Geology* 23, 657–660.
- Jambor, J.L., Dutrizac, J.E., 1998. Occurrence and constitution of natural and synthetic ferrihydrite, a widespread iron oxyhydroxide. *Chem. Rev.* 98, 2549–2585.
- Jannasch, H.W., Wirsén, C.O., 1981. Morphological survey of microbial mats near deep-sea thermal vents. *Appl. Environ. Microbiol.* 41, 528–538.
- Johnson, K.T.M., Graham, D.W., Rubin, K.H., Nicolaysen, K., Scheirer, D.S., Forsyth, D.W., Baker, E.T., Douglas-Priebe, L.M., 2000. Boomerang Seamount: the active expression of the Amsterdam–St. Paul hotspot, Southeast Indian Ridge. *Earth Planet. Sci. Lett.* 183, 245–259.
- Juniper, S.K., Bird, D.F., Summit, M., Vong, M.P., Baker, E.T., 1998. Bacterial and viral abundances in hydrothermal event plumes over northern Gorda Ridge. *Deep-Sea Res.* II 45, 2739–2749.
- Kamenov, G.D., Perfit, M.R., Mueller, P.A., Jonasson, I.R., 2008. Controls on magmatism in an island arc environment: study of lavas and sub-arc xenoliths from the Tabar–Lihir–Tanga–Feni island chain, Papua New Guinea. *Contrib. Mineral. Petrol.* 155, 635–656.
- Kamenov, G.D., Dekov, V.M., Willingham, A.L., Savelli, C., Belluci, L.G., 2009. Anthropogenic Pb in recent hydrothermal sediments from the Tyrrhenian Sea: implications for seawater Pb control on low-temperature hydrothermal systems. *Geology* 37, 111–114.
- Karl, D.M., 1995. Ecology of free-living, hydrothermal vent microbial communities. In: Karl, D.M. (Ed.), *The Microbiology of Deep-Sea Hydrothermal Vents*. CRC Press, N.Y., pp. 219–253.
- Kasama, T., Murakami, T., 2001. The effect of microorganisms on Fe precipitation rates at neutral pH. *Chem. Geol.* 180, 117–128.
- Kennedy, C.B., Martinez, R.E., Scott, S.D., Ferris, F.G., 2003a. Surface chemistry and reactivity of bacteriogenic iron oxides from Axial Volcano, Juan de Fuca Ridge, north-east Pacific Ocean. *Geobiology* 1, 59–69.
- Kennedy, C.B., Scott, S.D., Ferris, F.G., 2003b. Characterization of bacteriogenic iron oxide deposits from Axial Volcano, Juan de Fuca Ridge, northeast Pacific Ocean. *Geomicrobiol. J.* 20, 199–214.
- Kita, I., Taguchi, S., Matsubaya, O., 1985. Oxygen isotope fractionation between amorphous silica and water at 34–93 °C. *Nature* 314, 83–84.
- Klencsár, Z., Kuzmann, E., Vértes, A., 1996. User-friendly software for Mössbauer spectrum analysis. *J. Radioanal. Nucl. Chem.* 210, 105–118.
- Konhauser, K., 1998. Diversity of bacterial iron mineralization. *Earth Sci. Rev.* 43, 91–121.
- Lalonde, S.V., Konhauser, K.O., Reysenbach, A.-L., Ferris, F.G., 2005. The experimental silicification of Aquificales and their role in hot spring sinter formation. *Geobiology* 3, 41–52.
- Minshull, T.A., Bruguier, N.J., Brozena, J.M., 1998. Ridge-plume interactions or mantle heterogeneity near Ascension Island? *Geology* 26, 115–118.
- Murad, E., Cashion, J., 2004. *Mössbauer Spectroscopy of Environmental Materials and Industrial Utilization*. Kluwer Academic Publisher, Boston, pp. 159–223.
- Murad, E., Johnson, J.H., 1987. In: Long, G.L. (Ed.), *Iron oxides and oxyhydroxides. : Mössbauer Spectroscopy, Applied to Inorganic Chemistry*. Plenum Press, New York, pp. 507–574.
- Nakagawa, S., Takai, K., 2008. Deep-sea vent chemoautotrophs: diversity, biochemistry and ecological significance. *FEMS Microbiol. Ecol.* 65, 1–14.
- Perner, M., Seifert, R., Weber, S., Koschinsky, A., Schmidt, K., Strauss, H., Peters, M., Haase, K., Imhoff, J.F., 2007. Microbial CO<sub>2</sub> fixation and sulfur cycling associated with low-temperature emissions at the Lilliput hydrothermal field, southern Mid-Atlantic Ridge (9°S). *Environ. Microbiol.* 9, 1186–1201.
- Phoenix, V.R., Konhauser, K.O., Ferris, F.G., 2003. Experimental study of iron and silica immobilization by bacteria in mixed Fe–Si systems: implications for microbial silicification in hot-springs. *Can. J. Earth Sci.* 40, 1669–1678.
- Richards, M.A., Hager, B.H., Sleep, N.H., 1988. Dynamically supported geoid highs over hotspots: observation and theory. *J. Geophys. Res.* 93, 7690–7708.
- Ruddiman, W.F., Janecsek, T.R., 1989. In: Ruddiman, W.F., Sarnthein, M., et al. (Eds.), *Pliocene–Pleistocene biogenic and terrigenous fluxes at Equatorial Atlantic sites 662, 663, and 664. : Proceedings of the Ocean Drilling Program, Scientific Results*. Ocean Drilling Program, College Station, TX, pp. 211–240.
- Santelli, C.M., Orcutt, B.N., Bach, W., Moyer, C.L., Sogin, M.L., Staudigel, H., Edwards, K.J., 2008. Abundance and diversity of microbial life in oceanic crust. *Nature* 453, 653–656.
- Schmidt, M., Botz, R., Stoffers, P., Anders, T., Bohrmann, G., 1997. Oxygen isotopes in marine diatoms: a comparative study of analytical techniques and new results on the isotope composition of recent marine diatoms. *Geochim. Cosmochim. Acta* 61, 2275–2280.
- Schwertmann, U., Murad, E., 1983. Effect of pH on the formation of goethite and hematite from ferrihydrite. *Clays Clay Miner.* 31, 277–284.
- Spiess, F.N., Macdonald, K.C., Atwater, T., Ballard, R., Carranza, A., Cordoba, D., Cox, C., Diaz Garcia, V.M., Francheteau, J., Guerrero, J., Hawkins, J., Haymon, R., Hessler, R., Juteau, T., Kastner, M., Larson, R., Luyendyk, B., Macdougall, J.D., Miller, S., Normark, W., Orcutt, J., Rangin, C., 1980. East Pacific Rise: hot springs and geophysical experiments. *Science* 207, 1421–1433.
- Stevens, J.G., Pollak, H., Zhe, L., Stevens, V.G., White, R.M., Gibson, J.L., 1983. *Mössbauer Handbook, Mineral References and Mineral Data*. Mössbauer Effect Data Center, Asheville, pp. 103–104.
- Sudek, L.A., Templeton, A.S., Tebo, B.M., Staudigel, H., 2009. Microbial ecology of Fe (hydr)oxide mats and basaltic rock from Vailulu'u Seamount, American Samoa. *Geomicrobiol. J.* 26, 581–596.
- Sun, S.-S., McDonough, W.F., 1989. Chemical and isotopic systematics of oceanic basalts: implications for mantle composition and processes. In: Saunders, A.D., Norry, M.J. (Eds.), *Magmatism in the Ocean Basins: Geological Society of London, Special Publications*, 42, pp. 313–345.
- Takai, K., Nunoura, T., Horikoshi, K., Shibuya, T., Nakamura, K., Suzuki, Y., Stott, M., Massoth, G.J., Christenson, B.W., de Ronde, C.E.J., Butterfield, D.A., Ishibashi, J., Lupton, J.E., Evans, L.J., 2009. Variability in microbial communities in black smoker chimneys at the NW Caldera vent field, Brothers Volcano, Kermadec Arc. *Geomicrobiol. J.* 26, 552–569.
- Toner, B.M., Santelli, C.M., Marcus, M.A., Wirth, R., Chan, C.S., McCollom, T., Bach, W., Edwards, K.J., 2009. Biogenic iron oxyhydroxide formation at mid-ocean ridge hydrothermal vents: Juan de Fuca Ridge. *Geochim. Cosmochim. Acta* 73, 388–403.
- Ueshima, M., Tazaki, K., 2001. Possible role of microbial polysaccharides in nontronite formation. *Clays Clay Miner.* 49, 292–299.
- Urrutia, M.M., Beveridge, T.J., 1994. Formation of fine-grained silicate minerals and metal precipitates by a bacterial surface (*Bacillus subtilis*) and the implications in the global cycling of silicon. *Chem. Geol.* 116, 261–280.
- Usui, A., Bau, M., Yamazaki, T., 1997. Manganese microchimneys buried in the Central Pacific pelagic sediments: evidence of intraplate water circulation? *Mar. Geol.* 141, 269–285.
- Yapp, C.J., 1987. Oxygen and hydrogen isotope variations among goethites ( $\alpha$ -FeOOH) and the determination of paleotemperatures. *Geochim. Cosmochim. Acta* 51, 355–364.
- Yapp, C.J., 2007. Oxygen isotopes in synthetic goethite and a model for the apparent pH dependence of goethite-water <sup>18</sup>O/<sup>16</sup>O fractionation. *Geochim. Cosmochim. Acta* 71, 1115–1129.
- Yee, N., Phoenix, V.R., Konhauser, K.O., Benning, L.G., Ferris, F.G., 2003. The effect of cyanobacteria on silica precipitation at neutral pH: implications for bacterial silicification in geothermal hot springs. *Chem. Geol.* 199, 83–90.